U-Pb dating of interspersed gabbroic magmatism and hydrothermal metamorphism during lower crustal accretion, Vema lithospheric section, Mid-Atlantic Ridge

AGU PUBLICATIONS

JGR

Journal of Geophysical Research: Solid Earth

RESEARCH ARTICLE
10.1002/2014JB011668

Key Points:
- U-Pb dates constrain the timing of hydrothermal processes during crustal growth
- Crustal accretion included interspersed magmatism and hydrothermal alteration
- Lower crustal accretion occurred over a ~3.5–7 km zone

Supporting Information:
- Text S1
- Table S1
- Table S2

Correspondence to:
M. Rioux,
rioux@eri.ucsb.edu

Citation:
Rioux, M., N. Jöns, S. Bowring, C. J. Lissenberg, W. Bach, A. Kylander-Clark, B. Hacker, and F. Dudás (2015), U-Pb dating of interspersed gabbroic magmatism and hydrothermal metamorphism during lower crustal accretion, Vema lithospheric section, Mid-Atlantic Ridge, *J. Geophys. Res. Solid Earth*, *120*, 2093–2118, doi:10.1002/2014JB011668.

Received 6 OCT 2014
Accepted 11 MAR 2015
Accepted article online 16 MAR 2015
Published online 19 APR 2015

U-Pb dating of interspersed gabbroic magmatism and hydrothermal metamorphism during lower crustal accretion, Vema lithospheric section, Mid-Atlantic Ridge

Matthew Rioux[1,2], Niels Jöns[3,4,5], Samuel Bowring[1], C. Johan Lissenberg[6], Wolfgang Bach[3,4], Andrew Kylander-Clark[7], Bradley Hacker[2,7], and Frank Dudás[1]

[1]Department of Earth, Atmospheric, and Planetary Sciences, Massachusetts Institute of Technology, Cambridge, Massachusetts, USA, [2]Earth Research Institute, University of California, Santa Barbara, California, USA, [3]Department of Geosciences, University of Bremen, Bremen, Germany, [4]Marum Center for Marine Environmental Sciences, Bremen, Germany, [5]Department of Geology, Mineralogy and Geophysics, Ruhr-University Bochum, Bochum, Germany, [6]School of Earth and Ocean Sciences, Cardiff University, Cardiff, United Kingdom, [7]Department of Earth Science, University of California, Santa Barbara, California, USA

Abstract New U/Pb analyses of zircon and xenotime constrain the timing of magmatism, magmatic assimilation, and hydrothermal metamorphism during formation of the lower crust at the Mid-Atlantic Ridge. The studied sample is an altered gabbro from the Vema lithospheric section (11°N). Primary gabbroic minerals have been almost completely replaced by multiple hydrothermal overprints: cummingtonitic amphibole and albite formed during high-temperature hydration reactions and are overgrown first by kerolite and then prehnite and chlorite. In a previous study, clear inclusion-free zircons from the sample yielded Th-corrected $^{206}Pb/^{238}U$ dates of 13.528 ± 0.101 to 13.353 ± 0.057 Ma. Ti concentrations, reported here, zoning patterns and calculated Th/U of the dated grains are consistent with these zircons having grown during igneous crystallization. To determine the timing of hydrothermal metamorphism, we dated a second population of zircons, with ubiquitous <1–20 μm chlorite inclusions, and xenotimes that postdate formation of metamorphic albite. The textures and inclusions of the inclusion-rich zircons suggest that they formed by coupled dissolution-reprecipitation of metastable igneous zircon during or following hydrothermal metamorphism. Th-corrected $^{206}Pb/^{238}U$ dates for the inclusion-rich zircons range from 13.598 ± 0.012 to 13.503 ± 0.018 Ma and predate crystallization of all but one of the inclusion-free zircons, suggesting that the inclusion-rich zircons were assimilated from older hydrothermally altered wall rocks. The xenotime dates are sensitive to the Th correction applied, but even using a maximum correction, $^{206}Pb/^{238}U$ dates range from 13.341 ± 0.162 to 12.993 ± 0.055 Ma and postdate crystallization of both the inclusion-rich zircons and inclusion-free igneous zircons, reflecting a second hydrothermal event. The data provide evidence for alternating magmatism and hydrothermal metamorphism at or near the ridge axis during accretion of the lower crust at a ridge-transform intersection and suggest that hydrothermally altered crust was assimilated into younger gabbroic magmas. The results of this study show that high-precision U-Pb dating is a powerful method for studying the timing of magmatic and hydrothermal processes at mid-ocean ridges.

1. Introduction

Geologic evidence indicates that hydrothermal circulation plays an important role in cooling the lower crust at slow-spreading mid-ocean ridges. Gabbroic rocks with subgreenschist- to amphibolite-facies metamorphism, attributed to hydrothermal circulation, have been recovered from numerous exposures of lower crustal sections at slow-spreading ridges [e.g., *Bonatti et al.*, 1975; *Coogan et al.*, 2001b; *Fletcher et al.*, 1997; *Gillis et al.*, 1993; *Ito and Anderson*, 1983; *Mevel*, 1988; *Miyashiro et al.*, 1971; *Talbi et al.*, 1999]. Similarly, detailed studies of deep drill cores into lower crustal gabbros exposed by detachment faults (Atlantis Massif, Mid-Atlantic Ridge (MAR), and Atlantis Bank, Southwest Indian Ridge (SWIR)) have documented multiple generations of hydrothermal metamorphism, including high-temperature amphibolite-facies metamorphism attributed to fluid infiltration at or near the ridge axis [*Nozaka and Fryer*, 2011; *Robinson et al.*, 1991; *Stakes et al.*, 1991; *Vanko and Stakes*, 1991] and greenschist-facies and lower grade metamorphism related to cooling and exhumation [*Bach et al.*, 2001; *Beard et al.*, 2009; *Delacour et al.*, 2008; *Frost et al.*, 2008; *Nozaka and Fryer*, 2011; *Nozaka et al.*, 2008; *Robinson et al.*, 1991; *Stakes et al.*, 1991; *Vanko and Stakes*, 1991].

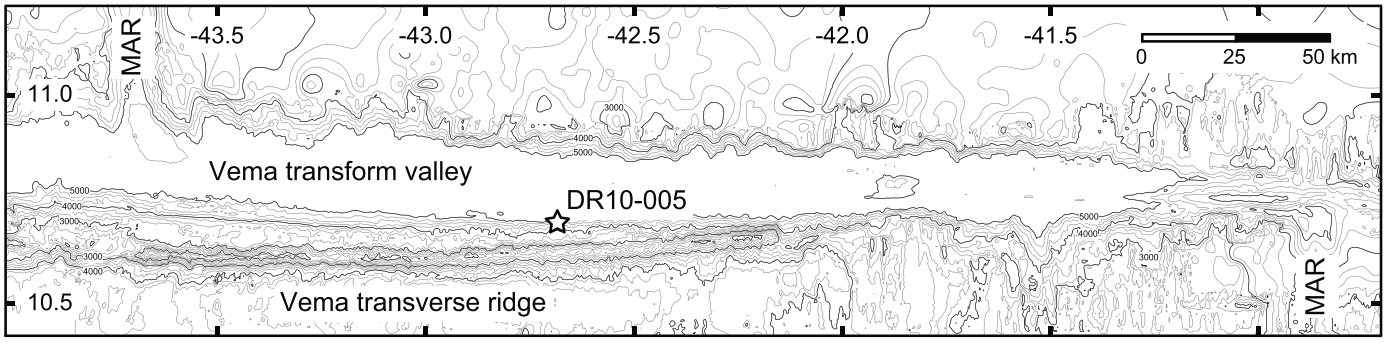

Figure 1. Bathymetric map of the Vema transform. The Vema lithospheric section is exposed on the northern side of the Vema transverse ridge. The transform offsets the Mid-Atlantic Ridge (MAR) to the west. The plotted sample location is the starting point of the dredge. Contour interval is 250 m, and contour depths are in meters below sea level. Contours derived from the Global Multi-Resolution Topography synthesis [*Ryan et al*., 2009] accessed through GeoMapApp. Figure after *Brunelli et al*. [2006].

To understand crustal accretion at slow-spreading ridges, it is necessary to understand the interaction between hydrothermal and magmatic processes, which is likely complex. Crustal growth at slow-spreading ridges is thought to occur by episodic magmatic intrusions, resulting in transitory thermal conditions and an evolving crustal structure [e.g., *Sinton and Detrick*, 1992]. Microseismicity indicates that during amagmatic intervals, faults at the ridge axis can penetrate into the lower crust [*Kong et al*., 1992; *Toomey et al*., 1985; *Wolfe et al*., 1995], facilitating deeper hydrothermal systems. If the overall cooling history of the crust is repeatedly perturbed by successive magmatic intrusions, gabbros in the lower crust could be affected by multiple generations of hydrothermal metamorphism [*Gillis et al*., 1993].

To determine the timing of magmatism and hydrothermal alteration during formation of the lower crust at a slow-spreading ridge, we applied high-precision geochronology to a hydrothermally metamorphosed gabbro from the Vema lithospheric section at 11°N on the MAR. The Vema lithospheric section is exposed along a ~300 km ridge on the southern side of the Vema transform fault (Figure 1) [*Auzende et al*., 1989; *Bonatti et al*., 2003; *Heezen et al*., 1964; *Kastens et al*., 1998]. The ridge rises 3–4 km above the transform valley, and the faulted northern side exposes a relatively undisturbed cross section through pillow basalts, sheeted dikes, gabbros, and mantle peridotites [*Auzende et al*., 1989]. The crust in the study area is thin, with a total thickness of ~2.2 km [*Auzende et al*., 1989]. The ridge was uplifted between 12 and 11 Ma, during a change in orientation of the MAR axis [*Bonatti et al*., 2005]. The studied sample was recovered by dredge during an R/V *Jean Charcot* cruise in 1978 [*Honnorez et al*., 1984].

In two previous studies, we have used high-precision U/Pb zircon geochronology to study the age and timescales of igneous crystallization in the Vema lithospheric section [*Lissenberg et al*., 2009; *Rioux et al*., 2012b]. In these studies, we analyzed clear zircons with few or no inclusions from five gabbros collected by dredge and submersible. Th-corrected $^{206}Pb/^{238}U$ dates ranged from 13.70 to 13.22 Ma and were interpreted to record the timing of igneous crystallization—dates reported throughout are recalculated from *Rioux et al*. [2012b] using the most recent calibration of the EARTHTIME ET535 tracer, the revised value of $^{235}U/^{238}U$ in zircon from *Hiess et al*. [2012], and a revised estimate for the Th/U of the magmas from which the zircons crystallized (effective Th/U = 2.63 ± 0.90), following *Rioux et al*. [2015]. The dated gabbros were collected over a distance of ~6 km perpendicular to the ridge axis, and the distance-versus-age relationship is consistent with the spreading rate predicted from marine magnetic anomalies [*Lissenberg et al*., 2009; *Müller et al*., 2008]. Zircons from four of the gabbros yielded a range of Th-corrected $^{206}Pb/^{238}U$ dates with maximum likelihood estimates of the overdispersion between 0.072 and 0.164 Ma, consistent with either protracted crystallization in a magma chamber/mush zone or inheritance of older grains from adjacent rocks [*Lissenberg et al*., 2009; *Rioux et al*., 2012b].

Two of the studied gabbros were affected by hydrothermal metamorphism, and subsequent work on these samples demonstrated that one of them (DR10-005; dredge location 10.692°N, 42.680°W; Figure 1) contains multiple U-bearing accessory minerals, which provided the opportunity to directly date the timing of both magmatic and hydrothermal processes. Th-corrected $^{206}Pb/^{238}U$ dates for clear inclusion-free zircons in this gabbro ranged from 13.528 ± 0.101 to 13.353 ± 0.057 Ma [*Lissenberg et al*., 2009; *Rioux et al*., 2012b]. The additional U-bearing trace minerals include (1) a second zircon population with ubiquitous <1–20 μm chlorite

inclusions and (2) xenotimes ($Y[PO_4]$) that textural relationships suggest grew either during or following hydrothermal metamorphism. Here we present the results of a detailed study of this gabbro, including petrographic and geochemical constraints on the conditions of hydrothermal metamorphism, high-precision U-Pb dates for the inclusion-rich zircons and the xenotimes, and new Ti-in-zircon analyses of the previously dated clear zircons. The data suggest that there was interspersed hydrothermal metamorphism and gabbroic magmatism during formation of the gabbroic crust of the MAR along the Vema transform.

2. Analytical Techniques

Analytical work for this study was carried out at the Massachusetts Institute of Technology (MIT), the University of Kiel, the University of Bremen, and the University of California, Santa Barbara (UCSB).

2.1. Petrography

Petrographic relationships and mineral zoning were studied using scanning electron microscopy (SEM), and backscattered electron (BSE) and cathodoluminescence (CL) imaging. Imaging of major minerals was done on the JEOL Superprobe JXA-8900 in the Department of Geosciences, University of Kiel. Detailed imaging of zircon and xenotime was done in thin section, thick section, and grain mount on the JEOL Superprobe JXA-733 at MIT and on the FEI Quanta 400F field-emission SEM at UCSB.

2.2. Mineral Chemistry

Mineral chemistry was analyzed on the JEOL Superprobe JXA-8900 at the University of Kiel. For measurement of accessory zircon, xenotime, britholite, and monazite an accelerating voltage of 20 kV and a probe current of 60 nA were used. Prior to measurement, the internal structure of the mineral grains was carefully checked using BSE images. Standards for Si, Mg, Ca, Zr, Ti, Pb, and Th were natural minerals (zircon, forsterite, wollastonite, rutile, crocoite, and thorianite); synthetic U-bearing glass was used as a standard material for U, Hf metal for Hf, and synthetic orthophosphates [*Jarosewich and Boatner*, 1991] for the rare earth elements (REE), Y and P. The interference of Th Mγ on U Mβ was corrected using an experimentally determined correction factor. The JEOL ZAF procedure was used for matrix correction of the raw data. Major primary and secondary silicate and oxide minerals were measured using an accelerating voltage of 15 kV at a beam current of 15 nA. Natural minerals were used as reference materials, and the raw data were corrected using the JEOL ZAF procedure.

Complementary major mineral trace element analyses were performed by laser ablation-inductively coupled plasma-mass spectrometry (LA-ICP-MS) at the University of Bremen. We used a NewWave UP193 solid-state laser with an output wavelength of 193 nm, coupled to a ThermoScientific Element2 high-resolution ICP-MS. Depending on the microtextural context, the laser beam diameter was in the range of 40 to 100 μm. Ca or Si was used as an internal standard element for quantification of the raw data. National Institute of Standards and Technology (NIST) glass standard SRM612 was used for calibration; the analytical quality was controlled by repeat analyses of the glass standards NIST SRM610 and U.S. Geological Survey BCR-2G and BHVO-2G.

2.3. Ti-in-Zircon

Ti-in-zircon was measured by laser ablation using a Photon Machines 193 nm excimer laser with HelEx cell connected to a Nu Attom single-collector ICP-MS in the Department of Earth Science at UCSB. Analyses were standardized to 91500 zircon. To calibrate the fragment of 91500 used, we analyzed $^{49}Ti/^{29}Si$ of the fragment and NIST 612 glass using a 70 μm spot in linkscan mode. The UCSB 91500 fragment had Ti concentrations of 4.9 ± 0.7 ppm to 6.5 ± 0.7 ppm ($n = 8$) with a weighted mean of 5.8 ± 0.3 (mean square of weighted deviates (MSWD) = 2.2). The MSWD of the weighted mean is higher than expected for a single population, suggesting that either the estimated uncertainties are too small or 91500 is zoned in Ti, as suggested by *Watson et al.* [2006]. The range of measured Ti concentrations is consistent with measurements of Ti in other fragments of 91500 by *Watson et al.* [2006] (3–6 ppm), *Reid et al.* [2011] (4.1–5.9 ppm), and *Fu et al.* [2008] (3.1–7.0 ppm). ^{49}Ti in unknowns was measured on the Attom in static collection mode using a 50 μm laser spot. Zircons from GJ1 and the Bishop Tuff were used to monitor accuracy. GJ1 zircons analyzed during the sample analyses yielded Ti concentrations with a weighted mean of 4.5 ± 0.1 ppm (MSWD = 0.6; $n = 10$), within uncertainty of the Ti concentration for GJ1 determined relative to NIST612 during the standard calibration runs (4.7 ± 0.2 ppm; MSWD = 1.4; $n = 7$, one analysis excluded). Three analyses of Bishop Tuff zircons yielded Ti concentrations of 3.5 ± 0.3 ppm to 3.7 ± 0.3 ppm, in general agreement with Ti concentrations in Bishop Tuff zircons reported by *Reid et al.* [2011].

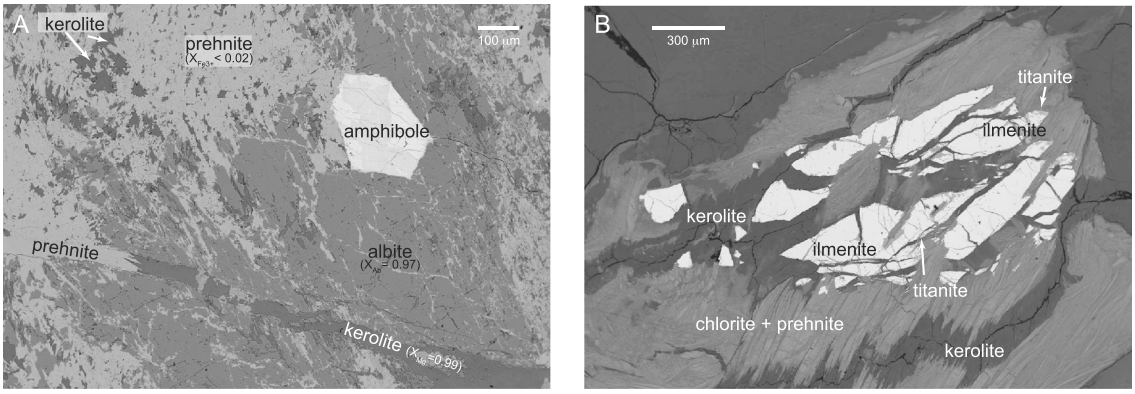

Figure 2. Backscattered electron (BSE) images of Vema gabbro DR10-005. (a) Cummingtonitic amphibole in a matrix of almost-pure albite. The assemblage is successively overprinted by end-member kerolite ($X_{Mg} = 0.99$) and chlorite + prehnite ($X_{Fe3+} < 0.02$). (b) Fractured ilmenite, locally overgrown by titanite. Chlorite + prehnite overgrow previously formed kerolite.

2.4. U-Pb Geochronology

U/Pb geochronology was carried out by isotope dilution-thermal ionization mass spectrometry (TIMS) in the radiogenic isotope lab at MIT. The analyzed zircons were separated and handpicked using standard mineral separation techniques. Representative grains were mounted, polished, and imaged by CL and BSE. The analyzed grains include both imaged grains that were plucked out of the mounts and whole unimaged grains. The analyzed xenotimes were first identified and imaged in polished slabs of the sample using BSE and then plucked individually from the slabs, allowing us to date grains with known petrographic contexts. Digestion and mass spectrometry procedures followed *Rioux et al*. [2012b]. Single grains and grain fragments of zircon were dissolved following the chemical abrasion method, which employs a two-step digestion process to isolate low U portions of the zircons, minimizing the impact of Pb loss [*Mattinson*, 2005]. In our previous analyses of clear inclusion-free zircons, we used a single 12–14 h leach step at 180–220°C; however, because of the small effective grain size between inclusions in the inclusion-rich zircons, in this study we used multiple 3–4 h leach steps at 180°C, for a total duration of 8–14 h. We rinsed the zircons between each step and inspected them under a microscope to determine how much material was left.

Xenotime grains were loaded into clean Savillex Teflon hex beakers, rinsed with H_2O, placed in an ultrasonic in acetone for ~15 min and then left at room temperature for ~12 h. The acetone was then removed, the grains were rinsed 2 times in H_2O and then left in Seastar hydrogen peroxide at room temperature for ~6 h. The grains were then rinsed in H_2O 3 times and loaded into clean Teflon microcapsules. Final digestion and column procedures were the same as for zircon. The xenotime rinse procedures were designed to remove residual carbon coating, from imaging of the grains, and other surface contamination without impacting the U-Pb systematics.

Isotopic analyses were carried out on a VG sector 54 TIMS at MIT. All data reduction, error propagation, and plotting of U-Pb data were done using the Tripoli and U-Pb_Redux software packages [*Bowring et al*., 2011; *McLean et al*., 2011], with the exception of the ^{234}U corrections, which were done off-line. Analyses were corrected for laboratory blank using the isotopic composition from repeat measurements of total procedural blanks reported in *Rioux et al*. [2012b].

3. Results

3.1. Major Mineral Petrography and Geochemistry

The studied gabbro from the Vema fracture zone underwent extensive hydrothermal alteration during a polyphase down-temperature evolution. Some primary textures and grain shapes still reflect the magmatic origin of the rock, but almost no primary magmatic minerals are preserved. Low Ti amphiboles of cummingtonitic to gruneritic composition ($X_{Mg} = Mg/(Mg + Fe) = 0.45–0.75$; Si = 7.5–7.92 per formula unit (p.f.u.), formula based on 23 oxygen atoms; Table S1 in the supporting information) preserve evidence of an early phase of high- temperature hydrothermal metamorphism (Figure 2a). Amphibole REE patterns are convex up, depleted in light REEs, and have a pronounced negative Eu anomalies (Table S1). REE concentrations are up to 1000 times

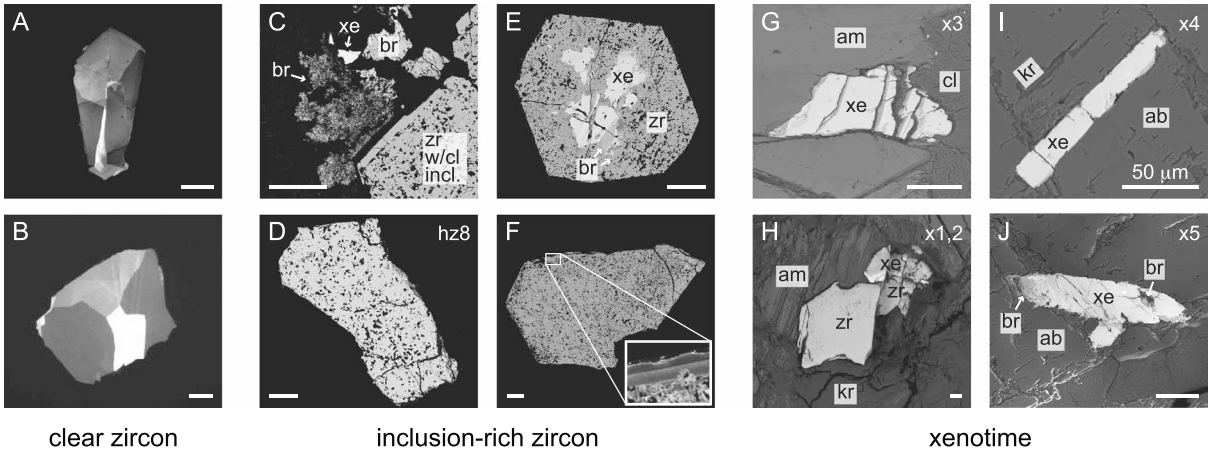

Figure 3. Backscattered electron (BSE) and cathodoluminescence (CL) images of U-bearing minerals from DR10-005. (a and b) CL images of clear zircons with few or no inclusions. (c–f) BSE images of inclusion-rich zircons. These zircons are locally associated with or intergrown with xenotime and britholite. The inset in Figure 3f is a close-up CL image of a thin coherent zircon rim that surrounds part of the grain. (g–j) BSE images of in situ xenotime. Grains that were plucked out and dated after imaging are labeled in the upper right corner (e.g., hz8 and x3), and the numbers correspond to the fraction numbers in Figures 5 and 6 and Table 2. Mineral abbreviations are the following: ab, albite; am, amphibole; br, britholite; cl, chlorite; kr, kerolite; zr, zircon; and xe, xenotime. The white bar in each figure is 50 μm.

chondritic values. Albite ($X_{Ab} = 0.96–1.00$, $X_{An} \leq 0.02$, $X_{Or} \leq 0.02$; Table S1) forms straight grain boundaries with cummingtonite, suggesting coeval formation; however, it is also possible that pseudomorphic albitization of more calcic igneous or metamorphic plagioclase occurred subsequent to cummingtonite formation. A final early mineral is ilmenite, which is locally fractured and overgrown by later titanite; the ilmenite may be a relict igneous mineral (Figure 2b).

Minerals formed during lower temperature hydrothermal metamorphism include kerolite, prehnite, and chlorite (Figure 2). Almost nickel-free kerolite (Ni < 500 ppm) forms irregular patches and veins cutting the rock

Table 1. Ti-in-Zircon Concentrations and Model Temperatures for Inclusion-Free Zircons From DR10-005

	Ti (ppm)	±2σ (abs)	T (°C)[a] $a_{TiO2} = a_{SiO2}$	T (°C)[a] $a_{TiO2} = 0.5$ $a_{SiO2} = 1$	T (°C)[a] $a_{TiO2} = 1$ $a_{SiO2} = 0.5$
iz7	5.13	0.35	687	748	632
iz8-1	9.48	0.61	741	810	680
iz8-2	12.00	0.76	763	835	700
iz9	11.04	0.70	755	826	693
iz11	6.92	0.45	712	777	655
iz12-3	5.90	0.42	699	762	643
iz12-4	8.73	0.55	733	801	673
iz14	7.72	0.51	722	788	664
iz16	9.84	0.62	744	814	683
iz17-1	11.78	0.75	761	833	698
iz17-2	9.64	0.61	742	811	682
iz18	11.34	0.69	758	829	695
iz19	9.90	0.63	745	814	684
iz20	11.96	0.77	763	835	700
iz21	9.69	0.59	743	812	682
iz22-3	9.91	0.62	745	814	684
iz23-3	7.30	0.47	717	783	659
iz23-4	8.48	0.50	731	798	671
iz24-1	6.47	0.39	706	770	650
iz24-2	10.57	0.63	751	821	689
iz25	6.92	0.43	712	777	655

[a]Temperatures calculated following *Ferry and Watson* [2007].

Table 2. Zircon and Xenotime U-Pb Data

	Inclusion-Rich Zircon							
	hz3	hz4	hz5	hz6	hz8	hz9	hz10	hz11
Pb^*/Pb_c[a]	9.2	57.4	20.9	11.1	19.5	12.0	10.1	3.8
Pb^* (pg)[b]	4.16	17.00	10.48	4.97	9.23	4.00	3.87	2.18
Pb_c (pg)[b]	0.45	0.30	0.50	0.45	0.47	0.33	0.38	0.57
Th/U[c]	0.065	0.058	0.052	0.064	0.056	0.069	0.069	0.091
$^{206}Pb/^{204}Pb$[d]	646.4	3934.1	1445.9	776.6	1350.5	834.8	705.7	275.4
$^{208}Pb/^{206}Pb$[d]	0.021	0.019	0.017	0.020	0.018	0.022	0.022	0.029
Uncorrected								
$^{206}Pb/^{238}U$[e]	0.0020930	0.0020973	0.0020970	0.0020828	0.0020925	0.0020914	0.0020892	0.0020934
$\pm 2\sigma$ %	0.14	0.060	0.079	0.13	0.087	0.13	0.16	0.31
$^{207}Pb/^{235}U$[e]	0.01337	0.013564	0.01363	0.01348	0.01321	0.01361	0.01331	0.01373
$\pm 2\sigma$ %	1.8	0.34	0.78	1.5	0.90	1.5	2.0	4.2
$^{207}Pb/^{206}Pb$[e]	0.04637	0.04693	0.04715	0.04697	0.04580	0.04722	0.04624	0.0476
$\pm 2\sigma$ %	1.8	0.33	0.76	1.5	0.89	1.4	1.9	4.1
Rho[f]	0.335	0.240	0.267	0.329	0.229	0.418	0.482	0.361
$^{206}Pb/^{238}U$ date[g]	13.478	13.5058	13.504	13.413	13.475	13.468	13.453	13.481
$\pm 2\sigma$ abs	0.019	0.0082	0.011	0.017	0.012	0.018	0.021	0.042
$^{207}Pb/^{235}U$ date[g]	13.49	13.681	13.74	13.60	13.32	13.73	13.43	13.85
$\pm 2\sigma$ abs	0.24	0.046	0.11	0.20	0.12	0.20	0.27	0.57
$^{207}Pb/^{206}Pb$ date[g]	16	44.5	56	47	−14	59	9	78
$\pm 2\sigma$ abs	42	7.9	18	35	21	34	46	97
% discordance[h]	14	70	76	71	195	77	−45	83
Model 1	*Complete Th Exclusion, No Excess ^{234}U*							
$^{206}Pb/^{238}U$[e]	0.0021100	0.0021142	0.0021140	0.0020998	0.0021095	0.0021083	0.0021061	0.0021103
$\pm 2\sigma$ %	0.14	0.060	0.078	0.13	0.086	0.13	0.16	0.31
$^{207}Pb/^{206}Pb$[e]	0.04599	0.04655	0.04678	0.04659	0.04543	0.04684	0.04587	0.0472
$\pm 2\sigma$ %	1.8	0.33	0.76	1.5	0.89	1.4	1.9	4.1
Rho[f]	0.335	0.240	0.267	0.329	0.229	0.417	0.482	0.361
$^{206}Pb/^{238}U$ date[g]	13.587	13.6148	13.613	13.522	13.584	13.577	13.562	13.589
$\pm 2\sigma$ abs	0.019	0.0082	0.011	0.017	0.012	0.018	0.021	0.042
$^{207}Pb/^{206}Pb$ date[g]	−4	25.3	37	27	−34	40	−10	59
$\pm 2\sigma$ abs	42	8.0	18	35	22	34	46	97
% discordance[h]	457	46	63	51	140	66	233	77
Model 2	*Th/U Source = 0.375 ± 0.130, No Excess ^{234}U*							
$^{206}Pb/^{238}U$[e]	0.0021070	0.0021116	0.0021116	0.0020969	0.0021069	0.0021052	0.0021030	0.0021062
$\pm 2\sigma$ %	0.14	0.074	0.085	0.13	0.094	0.13	0.16	0.30
$^{207}Pb/^{206}Pb$[e]	0.04606	0.04661	0.04683	0.04666	0.04548	0.04691	0.04594	0.04730
$\pm 2\sigma$ %	1.8	0.33	0.77	1.5	0.89	1.4	1.9	4.1
Rho[f]	0.277	0.178	0.202	0.266	0.165	0.353	0.419	0.310
$^{206}Pb/^{238}U$ date[g]	13.568	13.598	13.598	13.503	13.568	13.557	13.542	13.563
$\pm 2\sigma$ abs	0.019	0.010	0.012	0.018	0.013	0.018	0.021	0.041
$^{207}Pb/^{206}Pb$ date[g]	0	28.2	39	31	−31	44	−7	63
$\pm 2\sigma$ abs	43	8.1	18	36	22	34	46	97
% discordance[h]	3278	52	66	56	144	69	305	79
Model 3[i]	*No Th Disequilibrium, $^{234}U/^{238}U = 6.2875 \times 10^{-5}$ (Modern Seawater)*							
$^{206}Pb/^{238}U$[e]	0.0020850	0.0020893	0.0020890	0.0020748	0.0020845	0.0020834	0.0020812	0.0020854
$\pm 2\sigma$ %	0.14	0.060	0.079	0.13	0.087	0.13	0.16	0.31
$^{207}Pb/^{206}Pb$[e]	0.04654	0.04711	0.04733	0.04715	0.04597	0.04740	0.04642	0.04777
$\pm 2\sigma$ %	1.8	0.33	0.76	1.5	0.89	1.4	1.9	4.1
$^{206}Pb/^{238}U$ date[g]	13.427	13.4545	13.453	13.361	13.424	13.417	13.402	13.429
$\pm 2\sigma$ abs	0.019	0.0082	0.011	0.017	0.012	0.018	0.021	0.042
$^{207}Pb/^{206}Pb$ date[g]	25	54	65	56	−5	69	18	87
$\pm 2\sigma$ abs	42	54	65	56	21	68	46	96
% discordance[h]	46	75	79	76	372	80	27	85

Table 2. (continued)

	Xenotime				
	x1	x2	x3	x4	x5
Pb^*/Pb_c[a]	3.0	9.4	8.1	1.5	6.3
Pb^* (pg)[b]	1.34	3.99	4.51	0.66	3.44
Pb_c (pg)[b]	0.44	0.43	0.56	0.44	0.55
Th/U[c]	0.560	0.983	0.910	2.527	2.251
$^{206}Pb/^{204}Pb$[d]	196.3	516.3	457.6	77.4	273.7
$^{208}Pb/^{206}Pb$[d]	0.181	0.317	0.294	0.815	0.727
Uncorrected					
$^{206}Pb/^{238}U$[e]	0.0020007	0.0020300	0.0020408	0.002055	0.0020403
$\pm 2\sigma$ %	0.43	0.17	0.19	1.2	0.30
$^{207}Pb/^{235}U$[e]	0.01257	0.01315	0.01319	0.0129	0.0132
$\pm 2\sigma$ %	6.0	2.2	2.4	17	4.2
$^{207}Pb/^{206}Pb$[e]	0.0456	0.04700	0.0469	0.0457	0.0468
$\pm 2\sigma$ %	5.9	2.1	2.3	17	4.1
Rho[f]	0.295	0.328	0.321	0.260	0.330
$^{206}Pb/^{238}U$ date[g]	12.884	13.073	13.142	13.23	13.139
$\pm 2\sigma$ abs	0.055	0.022	0.025	0.16	0.040
$^{207}Pb/^{235}U$ date[g]	12.69	13.26	13.30	13.0	13.27
$\pm 2\sigma$ abs	0.76	0.28	0.31	2.2	0.56
$^{207}Pb/^{206}Pb$ date[g]	−24	48	43	−21	37
$\pm 2\sigma$ abs	143	50	55	413	99
% discordance[h]	153	73	69	164	65
Model 1	*Complete Th Exclusion, No Excess ^{234}U*				
$^{206}Pb/^{238}U$[e]	0.0020176	0.0020470	0.0020577	0.002072	0.0020573
$\pm 2\sigma$ %	0.43	0.17	0.19	1.2	0.30
$^{207}Pb/^{206}Pb$[e]	0.0452	0.04661	0.0465	0.0453	0.0464
$\pm 2\sigma$ %	5.9	2.1	2.3	17	4.1
Rho[f]	0.295	0.328	0.321	0.260	0.330
$^{206}Pb/^{238}U$ date[g]	12.993	13.182	13.251	13.34	13.248
$\pm 2\sigma$ abs	0.055	0.022	0.025	0.16	0.040
$^{207}Pb/^{206}Pb$ date[g]	−45	28	23	−40	17
$\pm 2\sigma$ abs	143	51	55	415	99
% discordance[h]	129	53	42	133	24
Model 2	*Th/U Source = 0.7 ± 0.3, $^{234}U/^{238}U = 6.2875 \times 10^{-5}$ (Modern Seawater)*				
$^{206}Pb/^{238}U$[e]	0.001996	0.002015	0.002027	0.002001	0.001993
$\pm 2\sigma$ %	0.51	0.54	0.51	1.9	1.3
$^{207}Pb/^{206}Pb$[e]	0.04571	0.0474	0.0472	0.0469	0.0479
$\pm 2\sigma$ %	5.9	2.2	2.4	17	4.3
Rho[f]					
$^{206}Pb/^{238}U$ date[g]	12.85	12.98	13.06	12.9	12.8
$\pm 2\sigma$ abs	0.51	0.54	0.51	1.9	1.3
$^{207}Pb/^{206}Pb$ date[g]	−19	66	58	44	93
$\pm 2\sigma$ abs	143	52	56	418	103
% discordance[h]	169	80	78	70	86

[a] Ratio of radiogenic to common Pb.
[b] Total radiogenic Pb, common Pb and U (picograms).
[c] Th/U ratio calculated from $^{208}Pb/^{206}Pb$ and the $^{206}Pb/^{238}U$ date of the sample.
[d] Fractionation and spike-corrected isotopic ratios, reduced using EARTHTIME ET535 tracer calibration version 3.
[e] Fractionation, spike, and blank-corrected radiogenic isotope ratios. Laboratory blanks were corrected using $^{206}Pb/^{204}Pb = 18.416 \pm 0.698$, $^{207}Pb/^{204}Pb = 15.358 \pm 0.452$, and $^{208}Pb/^{204}Pb = 37.461 \pm 1.470$.
[f] Correlation coefficient of radiogenic $^{207}Pb^*/^{235}U$ and $^{206}Pb^*/^{238}U$.
[g] Dates (Ma) calculated using $^{238}U/^{235}U = 137.818$ [*Hiess et al.*, 2012] and decay constants of $^{238}U = 1.5513 \times 10^{-10}$ year^{-1} and $^{235}U = 9.8485 \times 10^{-10}$ year^{-1} [*Jaffey et al.*, 1971].
[h] % discordance = 100 − (100 × ($^{206}Pb/^{238}U$ date)/($^{207}Pb/^{206}Pb$ date)).
[i] Model 3 uncertainties do not include uncertainties in the Th/U of the source or the initial $^{234}U/^{238}U$ of the zircons.

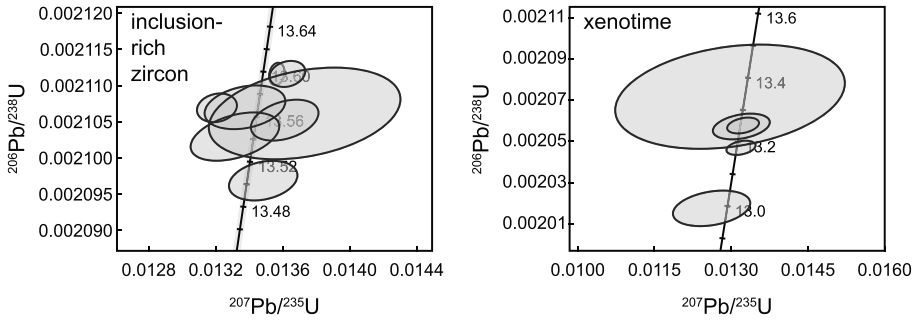

Figure 4. U-Pb concordia diagrams for single grain dates from the xenotimes and inclusion-rich zircons. Inclusion-rich zircon data are corrected assuming a Th/U of the source of 0.375 ± 0.130 (model 2). Xenotime data are corrected assuming complete Th exclusion and no ^{234}U disequilibrium. Ages on concordia are in Ma. Grey bands represent 2σ uncertainties on concordia based on decay constant uncertainties of 0.107% (^{238}U) and 0.136% (^{235}U) [*Jaffey et al.*, 1971]. Plots were generated using the U-Pb_Redux software package [*Bowring et al.*, 2011; *McLean et al.*, 2011].

and filling cracks. Analyzed grains have near Mg end-member composition ($X_{Mg} = 0.99$), contain minor CaO (0.4–0.5 wt %), Na_2O (0.05–0.25 wt %) and K_2O (~0.15 wt %), and some Al_2O_3 (1.4–2.1 wt %; Table S1). Mineral formulas calculated on the basis of 11 oxygen atoms show almost perfect talc stoichiometry; however, analysis totals are 86.6–89.0 wt % (Table S1), indicating a higher water content. The analysis totals are slightly lower than expected for kerolite [*Brindley et al.*, 1979, 1977] and may reflect intergrowth of kerolite with other hydrous phases (e.g., stevensite and smectite). Elevated Al_2O_3, K_2O, and MnO suggest incorporation of additional interlayer cations. While kerolite is not a recognized mineral name by the International Mineralogical Association, it has been identified and described in detail as a talc-like mineral with higher water content, wider basal spacing, and disordered layer stacking [*Brindley et al.*, 1977] and has been recognized as a low-temperature alteration phase in other hydrothermal system [*Dekov et al.*, 2008a, 2008b]. The exact mineral name applied does not impact the conclusions of this study regarding the conditions of hydrothermal alteration.

Prehnite and chlorite are pervasive, overgrow or replace all other minerals (cummingtonite, albite, and kerolite) and are interpreted to represent the latest stage of the hydrothermal alteration history. Prehnite aggregates are irregularly shaped and contain only minor iron ($Fe_2O_3 < 0.25$ wt %, assuming $Fe_{tot} = Fe^{3+}$; Table S1). The coexisting chlorite has a near Mg end-member composition ($X_{Mg} = 0.94$–0.99; Table S1). The small variability observed can be explained by Tschermak substitution.

3.2. Accessory Mineral Petrography and Geochemistry

Accessory minerals include zircon, xenotime, titanite, apatite, monazite, and britholite ($Ca_2[Y,Ce,Ca]_3[SiO_4,PO_4]_3[OH,F]$). The zircon and xenotime are the primary focus of this study. The clear zircons, dated by *Lissenberg et al.* [2009] and *Rioux et al.* [2012b], are characterized by sector zoning or an absence of zoning in CL, and many appear to be fragments of larger grains (Figures 3a, 3b, and S1). The inclusion-rich zircons contain ubiquitous <1–20 μm chlorite inclusions (Figures 3c–3f). Some grains have discontinuous segments of thin inclusion-free rims (Figures 3c and 3f), with clear CL zoning (Figure 3f). In situ inclusion-rich zircons are associated with or intergrown with xenotime and britholite (Figures 3c, 3e, and S2 and Table S2), and many grains also contain xenotime, britholite, and rare thorite ($[Th,U]SiO_4$) or coffinite ($[Th,U][SiO_4]_{1-x}[OH]_{4x}$) inclusions; the Th-U rich inclusions appear as small bright spots in Figure 3c and on the right termination of the zircon in Figure 3f. The xenotimes in the sample include grains associated with both clear and inclusion-rich zircons (Figures 3c, 3h, and S2) and isolated xenotimes in the groundmass (Figures 3g, 3i, and 3j). The britholite-(Y) associated with the inclusion-rich zircons and xenotimes is enriched in heavy REEs and has a trace element pattern similar to the xenotime. Analysis totals of britholite are low (Table S2), which may be due to water content or the porous texture of some grains.

Ti-in-zircon measurements were used to calculate model temperatures during zircon crystallization [*Ferry and Watson*, 2007; *Watson et al.*, 2006]. Ti concentrations in the clear zircons ranged from 5.1 to 12.0 ppm (Table 1; spot locations are marked in Figure S1). The Ti-in-zircon thermometer is dependent on the a_{SiO2}, a_{TiO2}, and P during crystallization. It is not possible to directly constrain the a_{SiO2} or a_{TiO2} in the studied sample because

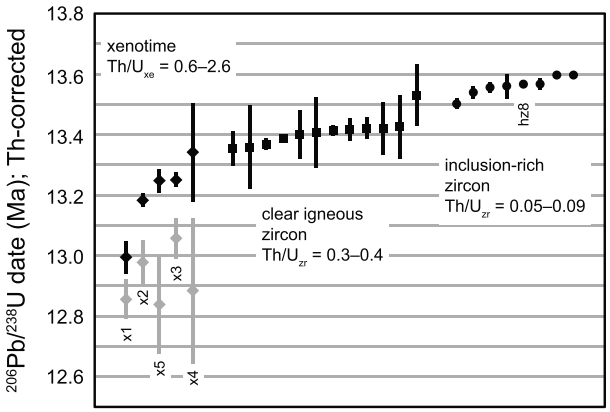

Figure 5. Preferred Th- and ^{234}U-corrected ^{206}Pb/^{238}U dates for zircons and xenotimes from sample DR10-005. Uncertainties are represented as 2σ confidence intervals. Clear igneous zircon dates are from *Lissenberg et al.* [2009] and *Rioux et al.* [2012b], recalculated using the most recent calibration of the EARTHTIME ET535 tracer, and Th corrected assuming a magma Th/U = 2.63 ± 0.90. Inclusion-rich zircon dates are corrected assuming a source Th/U = 0.375 ± 0.130 (model 2). Xenotime dates are maximum dates corrected assuming completed exclusion of ^{230}Th and no excess ^{234}U (black) and dates corrected using a parental liquid Th/U = 0.7 ± 0.3 and ^{234}U/^{238}U equivalent to modern seawater (grey). Th/U$_{xe}$ and Th/U$_{zr}$ refer to the calculated Th/U of the dated zircons and xenotimes.

almost all the igneous minerals have been replaced during hydrothermal metamorphism; however, a_{SiO2} and a_{TiO2} of most albite-bearing crustal rocks fall between 0.5 and 1.0 [*Ferry and Watson*, 2007]. The presence of early, potentially magmatic ilmenite and later titanite is consistent with $a_{TiO2} > 0.5$. Model Ti-in-zircon temperatures range from 687 to 763°C ($a_{TiO2} = a_{SiO2}$), 748 to 835°C ($a_{TiO2} = 0.5$, $a_{SiO2} = 1$), and 632 to 700°C ($a_{TiO2} = 1$, $a_{SiO2} = 0.5$). Assuming $a_{Ti02} < 0.5$ leads to higher model Ti-in-zircon temperatures. Estimated uncertainties on the model temperatures from the calibration fit are ± 11–16°C [*Ferry and Watson*, 2007]. The pressure dependence of the Ti-in-zircon thermometer has not been calibrated, but *Ferry and Watson* [2007] estimate an approximate variation of −50°C/GPa, for pressures below 1 GPa. The crust in the Vema section is thin (~2.2 km [*Auzende et al.*, 1989]), and the pressure dependence means that the model Ti-in-zircon temperatures reported above may be ~40–50°C too high. The heterogeneity in the 91500 standard leads to small ± 0.6–1.8 ppm uncertainties in the calculated Ti concentrations, corresponding to variations in the model Ti-in-zircon temperatures of ±10–16°C. It was not possible to measure Ti in the inclusion-rich zircons without the laser also hitting chlorite inclusions, and TiO_2 contents measured by electron microprobe could not be used for thermometry, because concentrations were near the detection limit.

Titanite, apatite, and monazite are less common and smaller than zircon and xenotime. Titanite occurs as narrow rims on ilmenite (Figure 2). Rare apatite grains are hypidiomorphic and show pronounced zonation in BSE images. Rare monazites are ≤ 30–40 μm long and show typical REE abundances (Table S2 and Figure S2). Variability in monazite REE + Y + P versus Th + U + Si shows scatter with some indication of brabantite

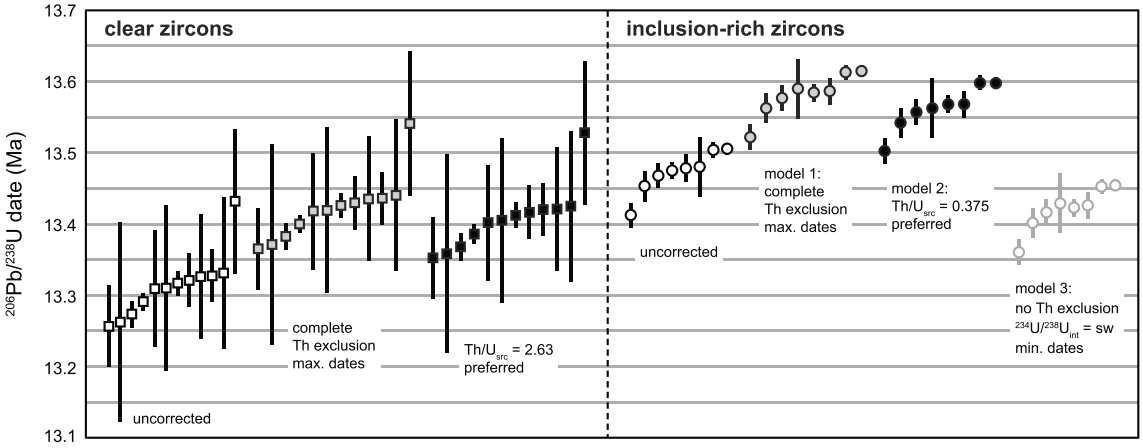

Figure 6. Comparison of different ^{230}Th and ^{234}U corrections for the inclusion-rich zircon and clear zircon dates. Maximum dates were calculated assuming complete exclusion of ^{230}Th during zircon crystallization. The three correction models for the inclusion-rich zircons are discussed in detail in the text. Model 3 uncertainties do not include uncertainties in the Th/U of the source or the initial ^{234}U/^{238}U of the zircons. Th/U$_{src}$ refers to the Th/U of the melt, fluid, or rock the zircon crystallized from (src, source). ^{234}U/^{238}U$_{int}$ = sw indicates an initial zircon U isotopic composition equal to modern seawater.

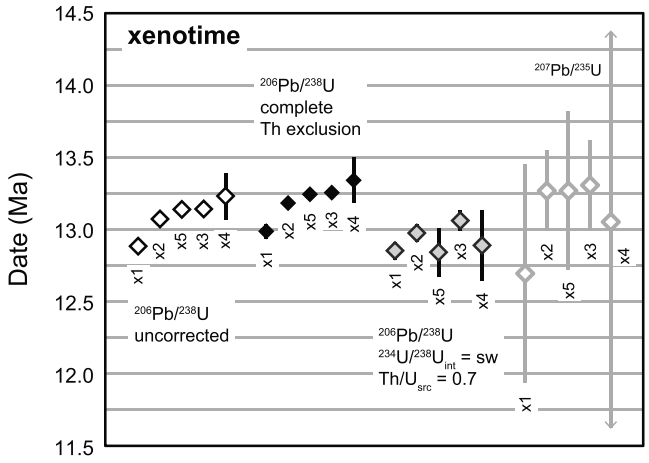

Figure 7. Comparison of different ^{230}Th and ^{234}U corrections for the xenotime data. The different correction models are discussed in detail in the text. $^{234}U/^{238}U_{int}$ = sw indicates an initial zircon U isotopic composition equal to modern seawater. The uncertainties in the $^{207}Pb/^{235}U$ date for grain x4 extend beyond the plot.

substitution. Near the rims, some monazite grains are replaced by another REE-rich mineral with a spongy texture, which may be britholite-(Ce).

3.3. Geochronology

Uncorrected $^{206}Pb/^{238}U$ dates for the inclusion-rich zircons and the xenotimes range from 13.506 ± 0.008 to 13.413 ± 0.017 Ma and 13.23 ± 0.16 to 12.884 ± 0.055 Ma, respectively (Table 2 and Figures 4–7). $^{207}Pb/^{235}U$ dates for the xenotimes range from 13.30 ± 0.31 to 12.69 ± 0.76 Ma. Both the inclusion-rich zircons and xenotimes had common Pb concentrations (Pb_c = 0.30–0.57 pg) that were indistinguishable from laboratory blanks (Table 2), suggesting that the initial leach steps effectively removed the inclusions prior to final digestion of the zircons and/or that any remaining inclusions in the zircons and any inclusions in the xenotimes contained little or no Pb_c. The analyzed inclusion-rich zircons also had very low Th/U, despite the presence of $[Th,U]SiO_4$ or $[Th,U][SiO_4]_{1-x}[OH]_{4x}$ inclusions in imaged grains, further suggesting that the leach steps effectively removed the inclusions in these grains.

For young samples, it is necessary to correct U/Pb dates for preferential inclusion or exclusion of intermediate daughter products in the ^{238}U and ^{235}U decay chains during crystallization or recrystallization of the analyzed mineral [*Mattinson*, 1973]. In the ^{238}U decay chain, two long-lived intermediate daughter products that can significantly impact the calculated dates are ^{230}Th ($t_{1/2}$ = 75,690 year) and ^{234}U ($t_{1/2}$ = 245,250 year) [*Cheng et al.*, 2000]. Initial ^{230}Th disequilibrium relative to ^{238}U is routinely corrected for using the Th/U of the dated phase and an estimated Th/U of the magma or fluid from which the phase crystallized. For ID-TIMS analyses, the Th/U of the dated phase is often calculated from the measured $^{208}Pb/^{206}Pb$ and $^{206}Pb/^{238}U$ date because Th is not routinely measured; uncertainties in model Th/U are likely negligible relative to other uncertainties in the Th corrections. Zircon typically excludes ^{230}Th relative to ^{238}U during crystallization and the maximum correction—assuming complete ^{230}Th exclusion—is +109,000 years; there is no upper limit to the correction for phases that incorporate excess Th. ^{234}U disequilibrium is less common; however, modern seawater is enriched in ^{234}U relative to secular equilibrium [*Andersen et al.*, 2010; *Chen et al.*, 1986a; *Delanghe et al.*, 2002], and analyses of seafloor hydrothermal systems and hydrothermally metamorphosed rocks indicate that seawater U is likely incorporated into mafic and ultramafic rocks during hydrothermal metamorphism [*Bach et al.*, 2001; *Bach et al.*, 2003; *Chen et al.*, 1986b; *Ludwig et al.*, 2011; *Michard and Albarede*, 1985; *Staudigel et al.*, 1996]. If a mineral crystallized from a liquid with $^{234}U/^{238}U$ equivalent to modern seawater, the excess ^{234}U would result in measured $^{206}Pb/^{238}U$ dates ~50,000 years older than the true crystallization age. In the ^{235}U decay chain, the most important long-lived intermediate daughter product is ^{231} Pa ($t_{1/2}$ = 32,710 year) [*Robert et al.*, 1969]. A limited number of studies have shown evidence for large ^{231} Pa excesses in some zircons [*Anczkiewicz et al.*, 2001; *Parrish et al.*, 2003], and smaller amounts of excess ^{231} Pa may be common [*Rioux et al.*, 2015; *Schmitt*, 2007].

The previously dated clear zircons from sample DR10-005 have model Th/U = 0.31–0.39, calculated from the $^{208}Pb/^{206}Pb$ and $^{206}Pb/^{238}U$ date of the zircons [*Lissenberg et al.*, 2009; *Rioux et al.*, 2012b]. These values are similar to Th/U of zircons from other unaltered Vema gabbros and zircons from gabbros and felsic dikes and veins from Atlantis Bank on the Southwest Indian Ridge [*Baines et al.*, 2009; *Lissenberg et al.*, 2009; *Rioux et al.*, 2012b; *Schwartz et al.*, 2005]. Based on the Th/U and the CL zoning in these grains, we previously interpreted them as magmatic zircons, and the Ti-in-zircon temperatures measured in this study provide further support for that interpretation. The reported $^{206}Pb/^{238}U$ dates for these grains were therefore Th corrected assuming an effective magma Th/U equivalent to an average Th/U for mid-ocean ridge

basaltic (MORB) glasses corrected for observed initial excess ^{230}Th in MORB (Figures 5 and 6; 2.63 ± 0.90) [*Rioux et al*., 2015]; the applied magma Th/U value in this study is revised from *Rioux et al*. [2012b] to more accurately account for global MORB variations and incorporate the ^{230}Th correction. An alternate approach to Th correcting ^{206}Pb/^{238}U data is to apply a constant zircon-melt $D_{Th/U}$ to predict the Th/U of the parental magma [e.g., *Barboni and Schoene*, 2014; *Wotzlaw et al*., 2014]. Applying a constant $D_{Th/U} = 0.20$ [*Wotzlaw et al*., 2014] to correct the ^{206}Pb/^{238}U dates of the clear zircons changes the Th-corrected dates by ≤ 0.009 Ma. For the purposes of this study, we feel that it is more accurate to correct the data using the measured Th/U and (^{230}Th)/(^{238}U) of MORB glasses (parentheses denote activates). We note that although the analyzed zircons crystallized from magmas that are more evolved than MORB, it is unlikely that magmatic differentiation significantly changed the Th/U of the magmas, as discussed in the supporting information of *Rioux et al*. [2012b, 2015].

In contrast to the clear zircons, the inclusion-rich zircons have very low calculated Th/U = 0.05–0.09 (Table 2). These values suggest that the parental (source) liquid also had low Th/U or that Th was preferentially expelled from the zircons during recrystallization. The degree of initial ^{230}Th disequilibrium is poorly constrained, and we considered three models (Table 2 and Figure 6):

1. *Complete Th Exclusion During Zircon Crystallization*. This model leads to the oldest possible Th-corrected ^{206}Pb/^{238}U dates of 13.615 ± 0.008 to 13.522 ± 0.017 Ma.
2. *Source Th/U = 0.375*. A likely origin for the inclusion-rich zircons is dissolution and reprecipitation of metastable igneous zircons. In this case, the Th/U of the source is the Th/U of the original igneous zircon. Using the average Th/U of the igneous zircons from the five Vema gabbros we have studied as the parental composition (Th/U = 0.375 ± 0.130), results in Th-corrected ^{206}Pb/^{238}U dates for the inclusion-rich zircons of 13.598 ± 0.012 to 13.503 ± 0.018 Ma. If the igneous zircons had not reached secular equilibrium prior to hydrothermal metamorphism, the effective Th/U of the protolith zircons would have been lower and the Th-corrected ^{206}Pb/^{238}U dates of the inclusion-rich zircons would be intermediate between these values and the uncorrected ^{206}Pb/^{238}U dates (13.506 ± 0.008 to 13.413 ± 0.017 Ma).
3. *No ^{230}Th Disequilibrium and Initial Zircon ^{234}U/^{238}U Equivalent to Modern Seawater*. We used a ^{234}U/^{238}U = 6.2875×10^{-5} for modern seawater, which is the average of measured values from *Chen et al*. [1986a], *Delanghe et al*. [2002], and *Andersen et al*. [2010]. These initial conditions provide ^{234}U-corrected ^{206}Pb/^{238}U dates of 13.454 ± 0.008 to 13.361 ± 0.017 Ma, which we consider minimum dates for these zircons.

We favor the second model, based on evidence discussed in section 4.2, and these dates are plotted in Figure 5 and used hereafter when referring to Th-corrected ^{206}Pb/^{238}U dates for the inclusion-rich zircons.

In models 1 and 2, all of the inclusion-rich zircons are older than all but one of the clear inclusion-free zircons (Figures 5 and 6). In these models, we assumed zircon preferentially incorporates or retains U relative to Th. This assumption is consistent with the observation that most zircons have Th/U lower than whole rock values, and with estimated zircon-melt $D_{Th/U} \sim 0.2$ [e.g., *Bindeman et al*., 2006; *Blundy and Wood*, 2003; *Schmitt et al*., 2003; *Wotzlaw et al*., 2014]. We argue in section 4.2 that the inclusion-rich zircons formed by dissolution-reprecipitation of igneous zircons and Th is also typically expelled from zircon during these processes [*Tomaschek et al*., 2003].

Model 3 merits a more detailed discussion. ^{206}Pb/^{238}U dates for the inclusion-rich zircons corrected using this model overlap the range of Th-corrected ^{206}Pb/^{238}U dates for the clear zircons, although most of the inclusion-rich zircons are still older than the two youngest precisely dated clear zircons (z4 and z8). This model would require that all of the U in the inclusion-rich zircons was derived from seawater and that the zircons did not preferentially exclude Th relative to U, suggesting a $D_{Th/U} \sim 1$. There is evidence that under oxidizing conditions—where U can occur in the U^{5+} or U^{6+} oxidation state—zircon may preferentially incorporate Th relative to U ($D_{Th/U} \geq 1$) [*Bacon et al*., 2007; *Burnham and Berry*, 2012]; under these conditions, zircon may incorporate excess ^{230}Th during crystallization, leading to ^{206}Pb/^{238}U dates that are older than the true crystallization age of the zircon. However, we consider it unlikely that the zircon-melt $D_{Th/U}$ were ≥ 1 for the inclusion-rich zircons. These grains have very low Th/U (0.05–0.09), and if $D_{Th/U} \geq 1$, it would require that the parental liquid or rock had Th/U equal to or below these values. The inclusion-rich zircons contain inclusions of $[Th,U]SiO_4$ or $[Th,U][SiO_4]_{1-x}[OH]_{4x}$, which occur in both polymineralic inclusions and as isolated monomineralic inclusions completely surrounded by zircon in two dimensions. Semiquantitative energy dispersive spectrometry of these inclusions indicate that they have Th/U ~ 4, suggesting there was abundant Th and U available during zircon crystallization and that the parental liquid or rock did not have a

low Th/U—although a high Th parental rock or liquid could have a low Th/U, it would require unreasonably high whole rock or liquid U concentrations. It is also highly unlikely that all of the U in the zircons was derived from seawater because studies of hydrothermally altered rocks from mid-ocean ridges suggest maximum U addition of < 0.3 ppm in none carbonate phases, and the U content of the inclusion-rich zircons (minimum > 100–200 ppm) suggests higher parental U concentrations; maximum U contents from hydrothermally altered rocks are from *Bach et al*. [2001, 2003] and *Staudigel et al*. [1996] excluding samples with > 3 wt % CO_2. These observations suggest that model 3 significantly underestimates the true age of the inclusion-rich zircons.

Zircon textures within the sample are consistent with the geochronologic data that indicate that the inclusion-rich zircons predate the clear zircons. If the inclusion-rich zircons postdated the clear zircons, the clear zircons would have represented easy nucleation points for further zircon growth, as observed in previous studies of hydrothermal zircons [*Hoskin*, 2005; *Schaltegger et al*., 2005]; however, we found no evidence of inclusion-rich rims on clear zircons.

Each of the dated xenotimes are shown in situ in Figure 3. The dated xenotimes have a large range of calculated Th/U = 0.57–2.56 (Table 2), which may reflect either true variability in the Th/U of the xenotimes [e.g., *Schaltegger et al*., 2005] and/or Th-rich inclusions in some grains. The high Th/U suggest that some grains may have included excess initial ^{230}Th, making the corrected ^{206}Pb/^{238}U dates sensitive to the estimated composition of the parental liquid. Figures 5 and 7 compare maximum ^{206}Pb/^{238}U dates corrected assuming completed exclusion of ^{230}Th and no excess ^{234}U (black; 13.34 ± 0.16 to 12.993 ± 0.055 Ma) and ^{206}Pb/^{238}U dates corrected using a parental liquid Th/U = 0.7 ± 0.3 and ^{234}U/^{238}U equivalent to modern seawater (grey; 13.06 ± 0.51 to 12.85 ± 0.51 Ma). Even lower Th/U of the parental liquid leads to younger ^{206}Pb/^{238}U dates and a significant increase in the uncertainties. The ^{207}Pb/^{235}U dates for the xenotimes are less precise than the ^{206}Pb/^{238}U dates but are not affected by initial Th disequilibrium and therefore may provide a more accurate crystallization age for these grains (assuming there was little or no ^{231} Pa disequilibrium). ^{207}Pb/^{235}U dates for the xenotimes range from 13.30 ± 0.31 to 12.69 ± 0.76 Ma, and the three most precise dates range from 13.30 ± 0.31 Ma to 13.26 ± 0.28 Ma. The ^{207}Pb/^{235}U dates overlap the Th-corrected ^{206}Pb/^{238}U dates and suggest that the correct Th correction for the ^{206}Pb/^{238}U dates is within the range of the two models presented above (Figure 7); the ^{207}Pb/^{235}U dates are closest to the maximum Th-corrected ^{206}Pb/^{238}U dates calculated assuming complete Th exclusion, whereas the ^{206}Pb/^{238}U dates corrected using a parental liquid Th/U = 0.7 and ^{234}U/^{238}U equal to modern seawater overlap the younger limit of the ^{207}Pb/^{235}U uncertainties. The variable ^{206}Pb/^{238}U dates of the xenotimes may reflect either protracted growth or more likely variations in initial ^{230}Th disequilibrium in the ^{238}U decay chain. The maximum ^{206}Pb/^{238}U dates require that most or all of the xenotimes grew after both the inclusion-rich and clear zircons.

4. Discussion

4.1. Conditions of Hydrothermal Metamorphism

Major mineral textures and chemistry constrain the conditions of hydrothermal alteration of the studied sample. Amphiboles in gabbroic rocks can form under conditions ranging from high-temperature crystallization of hydrous silicate melts to high-temperature ($>$300°C) interaction of hydrous fluids with the oceanic crust [*Hacker et al*., 2003]. Calcic high-alumina amphibole with high concentrations of TiO_2 is typically interpreted to be of magmatic origin [e.g., *Bazylev et al*., 2001]. In contrast, subcalcic and low-Ti amphibole are more commonly associated with high-temperature or hydrothermal metamorphism [e.g., *Silantyev et al*., 2008]. The amphiboles in DR10-005 have metamorphic textures, and the low Ti concentrations and cummingtonitic compositions are consistent with formation during hydrothermal alteration. *Coogan et al*. [2001b] argued that the Nb content of amphiboles can be used to distinguish between magmatic and hydrothermal amphibole, where magmatic amphiboles have high Nb ($>$1 ppm) and hydrothermal amphiboles formed from an igneous protolith have low Nb ($<$1 ppm). The amphiboles in DR10-005 have high Nb (~30 ppm), which may indicate that they formed as pseudomorphic replacements of preexisting magmatic amphiboles. In the Atlantis Massif, Mid-Atlantic Ridge, the occurrence of cummingtonitic amphibole has been attributed to mobility of CaO and SiO_2 at temperatures exceeding amphibolite-facies metamorphism [*Blackman et al*., 2006].

The pronounced negative Eu anomaly of the amphiboles may point to coexisting plagioclase during formation or recrystallization. While plagioclase likely also formed during high-temperature hydrothermal

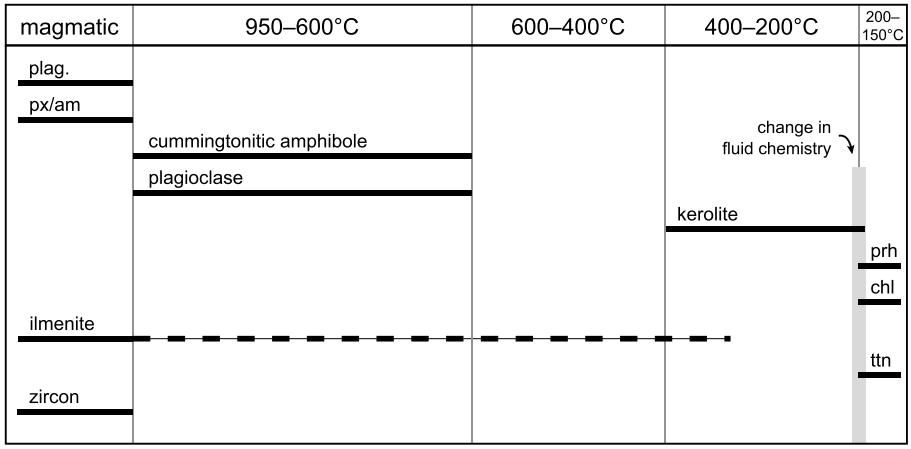

Figure 8. Sequence and estimated temperatures of hydrothermal mineral growth, based on mineral textures and chemistry. Abbreviations are the following: px, pyroxene; am, amphibole; prh, prehnite; chl, chlorite; and ttn, titanite.

metamorphism, the present albitic composition may be due to lower grade hydrothermal overprint. Given the uncertainty in the origin of the plagioclase composition, amphibole-plagioclase thermometry was not attempted. However, by analogy with other natural samples [e.g., *Coogan et al*., 2006; *Coogan et al*., 2001b; *Schroeder and John*, 2004] we make a temperature estimate of 600–950°C for growth of metamorphic plagioclase and amphibolite during high-temperature hydrothermal metamorphism (Figure 8).

The textures and compositions suggest that the observed kerolite formed in response to a brittle deformation event at temperatures below 500°C. *Eberl et al*. [1982] proposed the existence of a continuous structural series between talc, kerolite, and stevensite. Thermogravimetric heating experiments for kerolite show considerable weight loss between 100°C and 600°C and a pronounced decrease between 600°C and 800°C [*Brindley et al*., 1977]. The latter is likely due to release of OH, whereas the lower temperature weight loss, which is 70–100% reversible, is related to the interlayer breakdown. For stevensite, *DeRudder and Beck* [1963] proposed breakdown to talc at temperatures above 275°C. Derivation of kerolite formation temperatures from thermodynamic calculations is hindered by the random layer stacking and the resulting chemical variation; e.g., higher Al contents may point to an interstratified smectite component [*Dekov et al*., 2008b]. Oxygen isotope thermometry can be used to estimate the conditions of kerolite formation and *Dekov et al*. [2008a, 2008b] determined temperatures of 226–382°C for a kerolite-smectite assemblage and 153–207°C for chlorite in basalt and ultramafic hosted marine hydrothermal systems. Assuming a simple down-temperature evolution, the sequence of kerolite then chlorite fits our observation for the Vema sample. Based on the outlined constraints, we propose that focused high-temperature (200–400°C) fluid flow formed kerolite veins, before lower temperature, more pervasive flow lead to chlorite and prehnite growth (Figure 8).

Prehnite is an index mineral for the prehnite-pumpellyite facies [*Coombs et al*., 1959]. *Frey et al*. [1991] calculated the stability field of prehnite in the silica-saturated CaO-Al_2O_3-SiO_2-H_2O system to extend from 150 to 400°C. However, these authors noted that the size and pressure-temperature (*P-T*) extent of the stability field depend significantly on the coexisting minerals. Incorporation of trivalent iron can also shift the stability field to lower temperatures; however, the iron content is negligible in the Vema sample. Based on the Frey et al. study, the estimated temperatures of hydrothermal chlorite growth from the oxygen isotope thermometry by *Dekov et al*. [2008b], and the occurrence of prehnite in geothermal areas (*Rusinov* [1965], according to *Liou* [1971]), we estimate the prehnite + chlorite assemblage in the Vema sample formed at ~150–200°C.

4.2. Origin of the Zircons and Xenotimes

The CL zoning, model Th/U, and Ti contents of the inclusion-free clear zircons all suggest that they formed by igneous crystallization. The calculated Ti-in-zircon temperatures depend on the a_{TiO2} and a_{SiO2} and yield model temperatures of 630–840°C. The Ti-in-zircon concentrations and model crystallization temperatures are indistinguishable from zircons from mid-ocean ridge gabbros from Atlantis Massif (30°N, MAR), Atlantis Bank

(57°E, SWIR), and the Kane Fracture Zone (23°N, MAR), which record a continuous range of temperatures from 670 to 1020°C ($a_{TiO2} = 0.7$, $a_{SiO2} = 0.7$; $n = 406$) [*Grimes et al*., 2009; *John et al*., 2012]. The Th/U and zoning patterns in CL are also similar to other igneous zircons from the Vema lithospheric section [*Lissenberg et al*., 2009].

The textures of the inclusion-rich zircons suggest that these grains likely formed by dissolution-reprecipitation reactions. The inclusions in these zircons are primarily chlorite but also include smaller numbers of xenotime and britholite, and rare $[Th,U]SiO_4$ or $[Th,U][SiO_4]_{1-x}[OH]_{4x}$. *Tomaschek et al*. [2003] reported similar textures of zircons with numerous inclusions of Y, Th, and REE phases from high-pressure/low-temperature metamorphic rocks from Greece. These authors argued that the textures most likely formed as a result of Y, Th, and REE being expelled from the zircon structure during dissolution and reprecipitation [*Geisler et al*., 2007; *Tomaschek et al*., 2003]. The solubility of Y and Th in the zircon structure is temperature dependent, and magmatic zircons with high concentrations of these elements may be metastable at lower temperatures, providing a driving force for dissolution-reprecipitation [*Geisler et al*., 2007; *Tomaschek et al*., 2003]. The recrystallized zircons often have numerous small voids, which may reflect a volume change during the reaction [*Geisler et al*., 2007; *Tomaschek et al*., 2003]. The recrystallized zones are also characterized by lower Th/U and partially or completely reset U-Pb dates, suggesting preferential expulsion of Th and Pb relative to U.

Several studies suggest that similar dissolution-reprecipitation reactions can occur during hydrothermal metamorphism [*Grimes et al*., 2009; *Schwartz et al*., 2010; *Soman et al*., 2010; *Spandler et al*., 2004]. *Spandler et al*. [2004] described zircons in a schist from New Caledonia with inclusion-rich zones containing celadonite, kaolinite, quartz, Fe-oxy-hydroxide, smectite, chlorite, and Sc, Y, and REE phases. The low-temperature (<100°C) mineral assemblage and the presence of Sc, Y, and REE phases are consistent with dissolution-reprecipitation of igneous zircons during hydrothermal alteration of oceanic crust [*Spandler et al*., 2004]. The low-temperature inclusion assemblage in the zircons was preserved despite subsequent blueschist- to eclogite-facies metamorphism of the rock (1.6–1.9 GPa, >600°C). *Grimes et al*. [2009] and *Schwartz et al*. [2010] also documented zircons with porous domains and in some grains Y, Th, and U-rich inclusions from plutonic rocks from the MAR and the SWIR. These authors similarly interpreted the porosity, inclusions, and trace element contents of the zircons to reflect dissolution-reprecipitation either during hydrothermal or deuteric alteration.

In the inclusion-rich zircons from Vema, the xenotime and britholite inclusions suggest that the original zircon had high Y and REE concentrations and that these elements were expelled from the crystal structure during recrystallization. There are no preserved inclusion-free cores in these zircons that might represent unreacted igneous crystal. However, if the xenotime and britholite in the grain shown in Figure 3e were expelled from the zircon structure, a simple mass balance assuming spherical geometry suggests that the original zircon had Y contents > 1 wt %. Zones of unreacted zircon in the studies discussed above have similar Y contents [*Schwartz et al*., 2010; *Tomaschek et al*., 2003], and unreacted zircons with similar Y contents occur in other gabbros from the Vema section [*De Hoog et al*., 2014]. The low Th/U of the inclusion-rich zircons likely reflect preferential expulsion of Th relative to U during recrystallization [*Hoskin and Black*, 2000; *Rubatto et al*., 2008; *Tomaschek et al*., 2003]. The thin, inclusion-free rims with coherent zoning in CL on some grains (Figure 3f) may reflect either low-Y rims on the protolith zircons that did not undergo dissolution-reprecipitation or younger overgrowths that formed during subsequent magmatism or hydrothermal metamorphism. In previous studies of zircon textures attributed to dissolution-reprecipitation reactions, porous and inclusion-rich domains occur both as rims on unreacted cores and as cores with unreacted rims, likely reflecting the initial distribution of Y and other trace elements within the grains [*Schwartz et al*., 2010; *Tomaschek et al*., 2003].

Most of the imaged xenotimes appear to have grown during or following hydrothermal metamorphism. The most compelling evidence of this is xenotime X4, which grew parallel to the cleavage of metamorphic albite (Figure 3i). Other dated xenotimes were located along grain boundaries between metamorphic minerals. A few xenotimes are associated with both the inclusion-rich and clear inclusion-free zircons (Figures 3c and 3h); since zircon and xenotime are isostructural, the xenotime may have nucleated on existing zircons. In the case of the inclusion-rich zircons, the associated xenotime and britholite (Figure 3c) may be related to mobilization of Y from inclusions along the edges of the zircons or cracks within the zircons.

4.3. Interpretation of the U-Pb Dates

To understand the geologic significance of the dates from the inclusion-rich zircons and the observed intrasample variability, it is necessary to assess the potential impact of (i) the rims observed on some grains (Figures 3c and 3f), (ii) incomplete resetting during recrystallization, and (iii) Pb loss.

Most of the dated inclusion-rich zircons were not mounted and imaged prior to dating to preserve the maximum amount of material for analysis, and the extent of inclusion-free rims on these grains is not constrained. As discussed above, the rims could either be relic older zircon that did not undergo dissolution-reprecipitation or be younger rims that overgrew the reacted grains. In either case, several factors suggest that whereas the inclusion-free rims on some grains could explain some or all of the observed intrasample variability, either most of the dated zircons did not have rims or the rims did not have a significant impact on the zircon dates: (1) inclusion free rims were only observed on two of the six imaged grains; (2) the Th-corrected $^{206}Pb/^{238}U$ date for zircon hz8 (Figure 3d), which does not have a rim in BSE images, is within uncertainty of the dates of four other zircons (Figure 5 and Table 2); and (3) all of the dated inclusion-rich zircons have uniformly low Th/U, and there is no correlation between $^{206}Pb/^{238}U$ date and Th/U. Older or younger igneous rims would likely have higher Th/U, and if the rims had a significant impact on the measured $^{206}Pb/^{238}U$ date, they would also increase model Th/U for the zircons.

Incomplete resetting of the U-Pb system during zircon dissolution-reprecipitation could also impact the U-Pb isotopic systematics. However, the uniform, low Th/U of the dated zircons suggests that Th was effectively expelled from the crystal structure. Pb is less compatible than Th in zircon, making it likely that the U-Pb system was completely reset during dissolution-reprecipitation. This interpretation is supported by data from *Tomaschek et al.* [2003] and *Rubatto et al.* [2008], which show that zircons formed by dissolution-reprecipitation with uniformly low Th/U had reset U-Pb dates; not all recrystallized grains in these study were completely reset, but the spot analyses with slightly older U-Pb dates also had higher Th/U. *Hoskin and Black* [2000] reported partial resetting of U-Pb dates in recrystallized zircon with apparently reset Th/U ratios; however, textural evidence—including the preservation of relic igneous zoning in some recrystallized areas—suggests that the zircons in that study underwent solid-state recrystallization, rather than dissolution-reprecipitation, and this process appears to be less efficient at resetting the U-Pb system.

Although we consider it most likely that the U-Pb system was completely reset, we quantitatively assessed the impact of incomplete resetting. A key result of the U-Pb analyses is that the inclusion-rich zircons are older than the clear zircons. Given the evidence that the clear zircons have an igneous origin, we interpret the inclusion-rich grains or their protoliths to be older xenocrysts that were assimilated by a younger magma. To assess whether the dissolution-reprecipitation reactions occurred prior to or following assimilation, we used simple decay and mixing calculations. Given that Pb is less compatible than Th in zircon, we took the percentage of Th expelled as the minimum percentage of Pb expelled during the reactions. If the zircon protoliths to the inclusion-rich zircons had Th/U equal to the average Th/U of igneous zircons from the Vema gabbros (0.375) [*Lissenberg et al.*, 2009; *Rioux et al.*, 2012b], the low Th/U (0.05–0.09) of the inclusion-rich grains imply that 76–86% of the Th was expelled. Th-corrected $^{206}Pb/^{238}U$ dates for the inclusion-rich zircons range from 13.598 ± 0.012 to 13.503 ± 0.018 Ma, whereas the two youngest precisely dated clear inclusion-free zircons (z4 and z8) give a Th-corrected weighted mean $^{206}Pb/^{238}U$ date of 13.380 ± 0.011 Ma. If the dissolution-reprecipitation reactions occurred after crystallization of the younger magma, Pb was removed from the crystal structure at the same rate as Th, and the older dates of the inclusion-rich zircons are due to incomplete resetting of the U-Pb system, it would require that the protolith zircons are ≥ 0.72–1.57 Ma older than the clear zircons. This is a minimum estimate of the age of the protolith zircons because Pb is likely more incompatible that Th during zircon dissolution-reprecipitation reactions. Using the 16.1 km/Ma half-spreading rate calculated from marine magnetic anomalies [*Müller et al.*, 2008], the predicted age difference would correspond to 11.6 to 25.3 km of spreading. The similar age of the other gabbros we have dated from the Vema section [*Lissenberg et al.*, 2009; *Rioux et al.*, 2012b] suggests that the studied sample is not a dike or sill that intruded $\geq$12–25 km off axis, and we consider it unlikely that either a small fragment of older crust was trapped at the ridge axis for > 1.6 Ma or all of the dated gabbros are younger magmas intruding into a faulted older crustal block related to the adjacent transform. The latter conclusions are supported by the fact that we have not found ≥ 0.7–1.6 Ma xenocrystic zircons in any of the dated samples. Instead, the calculations suggest that the U-Pb system was reset by the dissolution-reprecipitation reactions, the Th-corrected $^{206}Pb/^{238}U$ dates reflect the timing of these reactions, and the dissolution-reprecipitation reactions occurred prior to assimilation of the inclusion-rich zircons into the younger gabbroic magma.

It is more difficult to quantitatively assess the impact of Pb loss on the dated inclusion-rich zircons. The numerous inclusions in these zircons reduce the effective grain size, increase surface area, and thus could facilitate Pb loss. The chemical-abrasion method minimizes the impact of Pb loss; however, because of the

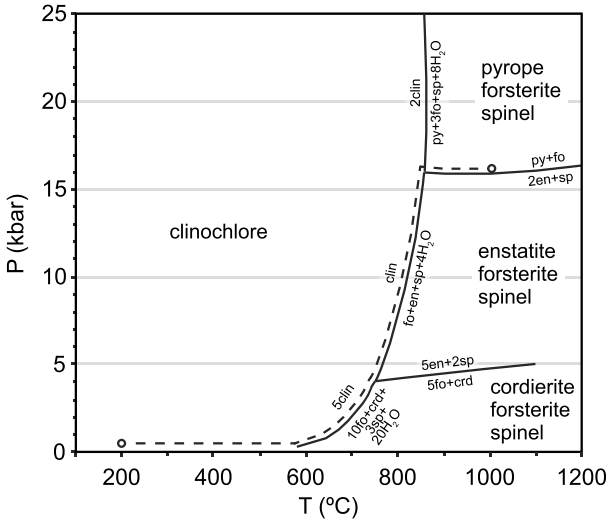

Figure 9. Phase diagram for Mg-chlorite (clinochlore) breakdown. The dashed line is the *P-T* path of chlorite inclusions in the inclusion-rich zircons during assimilation of the zircons into a 1000°C gabbroic magma, from a starting point of 0.5 kbar and 200°C. The elevated pressures in the inclusions result from the large volume increase associated with chlorite breakdown. Reaction positions were calculated using THERMOCALC 3.26 [*Powell and Holland*, 1988] and the *Holland and Powell* [1998] data set updated in November 2003 (tcds55.txt).

small effective grain size, we used shorter and lower temperature leach steps, which may not have removed all of the high-U zircon prior to final digestion. However, given the young age of the dated zircons, the moderate U contents (hundreds of parts per million), application of the chemical-abrasion method, and the overlapping dates for five of the eight dated zircons, it is unlikely that the $^{206}Pb/^{238}U$ dates for most grains are impacted by Pb loss. We also note that Pb loss would lead to $^{206}Pb/^{238}U$ dates that are younger than the true crystallization age of the zircons, such that the true age difference between the inclusion-rich and clear zircons would increase if Pb loss is a factor for the inclusion-rich zircons.

Based on the arguments above, we interpret the $^{206}Pb/^{238}U$ dates of the inclusion-rich zircons to primarily reflect the age of resetting of the U-Pb system during dissolution-reprecipitation reactions. We interpret the five intermediate Th-corrected $^{206}Pb/^{238}U$ dates (weighted mean = 13.5617 ± 0.0083 Ma; MSWD = 1.2)—which all overlap within uncertainty and include the rim absent grain hz8—as the best estimate of the age of the dissolution-reprecipitation reactions. The two older Th-corrected $^{206}Pb/^{238}U$ dates may be related to relic older rims, and the one younger Th-corrected $^{206}Pb/^{238}U$ date may reflect minor Pb loss. Following the dissolution-reprecipitation reactions, the inclusion-rich zircons were assimilated into the younger gabbroic magma and the clear igneous zircons crystallized from this magma. Using the average of the two youngest precise dates (z4 and z8) from the clear zircons as the best estimate of the final crystallization age of the younger magma (13.380 ± 0.011 Ma), the inclusion-rich zircons formed 0.162 ± 0.024 Ma to 0.218 ± 0.016 Ma prior to assimilation (excluding the youngest inclusion-rich date), and the protolith to the inclusion-rich zircon must have been ≥0.218 ± 0.016 Ma older.

Th-corrected $^{206}Pb/^{238}U$ dates of the xenotime from the sample are younger than the clear zircons (Figure 5), and textural evidence suggests that the xenotimes grew during hydrothermal metamorphism of the younger gabbro. The two oldest precise dates for the xenotime give an average Th-corrected $^{206}Pb/^{238}U$ of 13.251 ± 0.021 Ma (x3 and x5), assuming complete Th exclusion, indicating that the second hydrothermal metamorphism occurred ≥ 0.13 Ma after crystallization of the gabbro.

4.4. Origin of Chlorite Inclusions in the Inclusion-Rich Zircons

A final factor in understanding the geologic implications of the U-Pb dates of the inclusion-rich zircons is the origin of the ubiquitous chlorite inclusions in these grains. Previous studies of zircon textures attributed to dissolution-reprecipitation reactions have documented both pores/voids [*Geisler et al*., 2007; *Grimes et al*., 2009; *Rubatto et al*., 2008; *Schwartz et al*., 2010; *Tomaschek et al*., 2003] and mineral inclusions, including phases formed from elements purged from the zircon structure (e.g., xenotime and thorite) and metamorphic silicates (e.g., pyroxene, kaolinite, and chlorite) [*Rubatto et al*., 2008; *Spandler et al*., 2004]. For the inclusion-rich zircons in this study, the chlorite inclusions may have formed by hydrothermal alteration during or prior to the original dissolution-reprecipitation reactions, or during a later hydrothermal event.

A key consideration for understanding the origin of the chlorite inclusions is whether isolated chlorite inclusions, and the zircon containing them, could survive assimilation into a younger gabbroic magma. Chlorite breaks down to anhydrous minerals at magmatic temperatures, and the dehydration reactions have large volume increases that will lead to large internal pressures in isolated inclusions. If the internal pressures are high

enough, they could break apart the host zircon. Experimental studies have demonstrated that Mg-chlorite (clinochlore) breakdown reactions include the following:

$$5\ \text{clinochlore} = 10\ \text{forsterite} + \text{cordierite} + \text{Mg} - \text{spinel} + 20\ H_2O\ (P < 4\ \text{kbar}) \quad (1)$$

$$\text{clinochlore} = \text{forsterite} + \text{enstatite} + \text{Mg} - \text{spinel} + 4\ H_2O\ (4\ \text{kbar} < P < 16\ \text{kbar}) \quad (2)$$

$$2\ \text{clinochlore} = 3\ \text{forsterite} + \text{pyrope} + \text{Mg} - \text{spinel} + 8\ H_2O\ (P > 16\ \text{kbar}) \quad (3)$$

(Figure 9; pressure ranges are based on reaction pressure and temperatures calculated using THERMOCALC) [*Chernosky*, 1974; *Chernosky et al*., 1988; *Holland and Powell*, 1998; *Jenkins and Chernosky*, 1986; *Powell and Holland*, 1988; *Staudigel and Schreyer*, 1977].

To calculate the internal pressures generated by chlorite breakdown within an isolated inclusion in zircon, we calculated mineral volumes at pressure (P) and temperature (T) using the Tait equation of state and the thermodynamic data set of *Holland and Powell* [2011]. We used a starting condition of $P = 0.5$ kbar and $T = 200$°C, consistent with the temperature of chlorite formation during hydrothermal metamorphism and the thin 2.2 km thickness of the Vema crust. Final conditions of $T = 1000$°C and external $P = 0.5$ kbar were used to model assimilation of the zircon into a gabbroic magma. The initial volume of the inclusion was calculated as the molar volume of clinochlore at the initial conditions. The volume of the inclusion cavity would increase with increasing temperature, and we calculated this volume change based on the thermal expansion of zircon. To calculate the internal pressure generated by each of the chlorite-breakdown reactions, we calculated the volume of the solid reaction products at 0.5 kbar, 1000°C, and calculated the volume available for water liberated by the breakdown reactions as the difference between the volume of solid reaction products and the volume of the inclusion cavity at 1000°C. An initial estimate of the internal pressure of the inclusion was then calculated from the molar volume of water in the inclusion cavity, using the equation of state for water of *Pitzer and Sterner* [1995] (i.e., the water is constrained to the cavity volume, and the pressure is defined by the volume, molar amount of water, and temperature). The increased internal pressure from chlorite breakdown would deform the zircon and expand the inclusion cavity. To account for this expansion, we used equation (1) of *Guiraud and Powell* [2006], with the zircon shear modulus calculated at $P = 0.5$ kbar and $T = 1000$°C following *Hacker and Abers* [2004], using the shear moduli (G and G′) of *Özkan and Jamieson* [1978] or *Dutta and Mandal* [2012]. The *Guiraud and Powell* [2006] equation is not appropriate for areas with numerous closely spaced inclusions; however, the final *P-T* paths for the inclusions are not sensitive to the shear modulus. The elastic expansion of the inclusion cavity and a decrease in volume of the solid reaction products at increased internal pressure decreases the estimated internal pressure, making it necessary to iterate the calculations until an equilibrium internal pressure is determined.

At $T = 1000$°C and an external $P = 0.5$ kbar, the three breakdown reactions lead to theoretical internal pressures in isolated inclusions of 33.4 kbar (equation (1)), 21.5 kbar (equation (2)), and 9.2 kbar (equation (3)). However, because of the positive Clapeyron slope of the two lower pressure reactions (equations (1) and (2) and Figure 9), the high internal pressures predicted will not be reached. Instead, as temperature increases, the large pressure increases associated with equations (1) and (2) drive the *P-T* conditions back toward the chlorite side of the reactions, and the *P-T* paths of the inclusions follow the reaction *P-T* loci up to 16 kbar. Above 16 kbar, the stable reaction is equation (3), which leads to internal pressures below the pressure of the inclusions at that point. This will result in the *P-T* path of the inclusions following the 2enstatite + spinel = pyrope + forsterite reaction (Figure 9). The maximum internal pressures of the inclusions are therefore controlled by the position of the enstatite to pyrope reaction and will be ~16 kbar. This reaction is insensitive to temperature, and inclusion temperatures >1000°C will not significantly increase the internal pressures. Similarly, because of the large pressure drop associated with pyrope formation, even significant partial melting in the inclusions will not increase the internal pressures. *Parkinson and Katayama* [1999], using laser Raman microspectroscopy, found that coesite inclusions completely enclosed within zircon have internal pressures of 19–23 kbar. The pressures predicted here are significantly lower, suggesting that the inclusion-rich zircons could withstand chlorite breakdown in enclosed inclusions during assimilation into a younger gabbroic magma.

Given the large number and variable spacing of the inclusions in the studied zircons, it is likely that the stress fields of some inclusions would have interacted, possibly leading to brittle failure between inclusions. However, the calculations above suggest that a majority of the inclusions in the grains could have

remained isolated in the zircons during assimilation into a younger magma. At peak conditions, chlorite inclusions that had been incorporated into or grown in situ within the zircons would be converted to forsterite + spinel ± enstatite ± pyrope + water. The inclusions could subsequently revert back to chlorite along a reverse *P-T* path during crystallization of the magma and the subsequent cooling of the resultant gabbro. Diffusive loss of elements from the inclusions at magmatic temperatures is unlikely due to the slow diffusion rates in zircon [*Cherniak et al*., 1997; *Cherniak and Watson*, 2000]. A potential exception could be H due to its small radius; however, thermal decomposition of H_2O to H and O occurs at temperatures >1200°C [*Lede et al*., 1982], and H_2O diffusion is likely to be slower than O diffusion in zircon [*Watson and Cherniak*, 1997].

The chlorite inclusions occur throughout the zircons, and the vast majority of the inclusions, including submicron inclusions, are surrounded by zircons in two dimensions. We consider it most likely that many of these inclusions are completely isolated within the zircons and that the chlorite inclusions grew in situ or were incorporated into the zircons during the dissolution-reprecipitation reactions and followed the *P-T* path outlined above during assimilation of the zircons into the younger gabbroic magma. This interpretation is consistent with the results from *Spandler et al*. [2004], who argued that a low-temperature mineral assemblage, enclosed within zircons during dissolution-reprecipitation reactions, remained isolated even during subsequent high-pressure metamorphism. To further test this hypothesis, we attempted to compare the composition of the chlorite inclusions within the inclusion-rich zircons to the composition of the chlorite in the groundmass; however, due to the variable hardness of zircon and chlorite, a poor polish on the chlorite inclusions precluded accurate measurements of the composition.

Assimilation of the inclusion-rich zircons into the younger magma could have occurred as individual grains or within larger xenoliths. Alternately, the studied gabbro could represent a composite of the original older gabbro, cut by intrusive veins of younger gabbro. We did not observe any textural relationships that support the latter model, and we consider this unlikely; however, it is possible that original cross-cutting relationships have been obscured by the near complete hydrothermal metamorphism of the sample (supporting information Figure S3). The conclusions reached in this study are not dependent on the exact mechanism of interaction between the older gabbro that the inclusion-rich zircons formed in and the younger gabbro that intruded it.

An alternative explanation for the inclusion-rich zircon textures is that the dissolution-reprecipitation reactions that generated the inclusion-rich zircons generated numerous voids or pores within the grains. In this model, the dissolution-reprecipitation reactions may have been precipitated by either deuteric fluids related to the crystallization of the host magma or an adjacent younger magmatic intrusion or lower temperature hydrothermal fluids. Following assimilation of the porous zircons into a younger magma, these pores could have filled with chlorite during the same hydrothermal metamorphic event that generated the abundant chlorite in the samples groundmass. In this scenario, all of the original pores and voids within the zircons must have been interconnected, to allow later growth of chlorite throughout the grains. It is not possible to discount this hypothesis; however, we feel that the textural evidence is most consistent with the chlorite inclusions being isolated within the zircon and forming during a hydrothermal metamorphic event prior to assimilation into the younger gabbro.

4.5. Model of Lower Crustal Accretion

The combined textural, geochemical, and geochronologic data are consistent with interspersed magmatism and hydrothermal alteration at the ridge axis during lower crustal accretion. Our preferred explanation of the data (Figure 10) is (1) prior to 13.60 Ma, a gabbroic magma intruded and crystallized at the ridge axis. High-Y zircons formed during the final stages of gabbro crystallization. (2) The crystallized gabbro underwent hydrothermal alteration at temperatures as low as 150–200°C at ~13.56 Ma. The high-Y zircons were metastable and underwent dissolution-reprecipitation during or following the hydrothermal metamorphism, generating the inclusion-rich zircons. We consider it most likely that the ubiquitous chlorite inclusions formed within or were incorporated into the zircons at this time. (3) A second gabbroic magma intruded and partially assimilated the hydrothermally altered gabbro at ~13.38 Ma. The clear inclusion-free zircons crystallized from this younger magma. The occurrence of both inclusion-rich and clear inclusion-free zircons in a single sample suggests that the inclusion-rich zircons were assimilated into the younger magma as xenocrysts. (4) The younger gabbro underwent successive hydrothermal metamorphic events after 13.38 Ma, leading to the formation of the xenotime and the range of metamorphic assemblages preserved in the sample. The low-Y clear zircons would

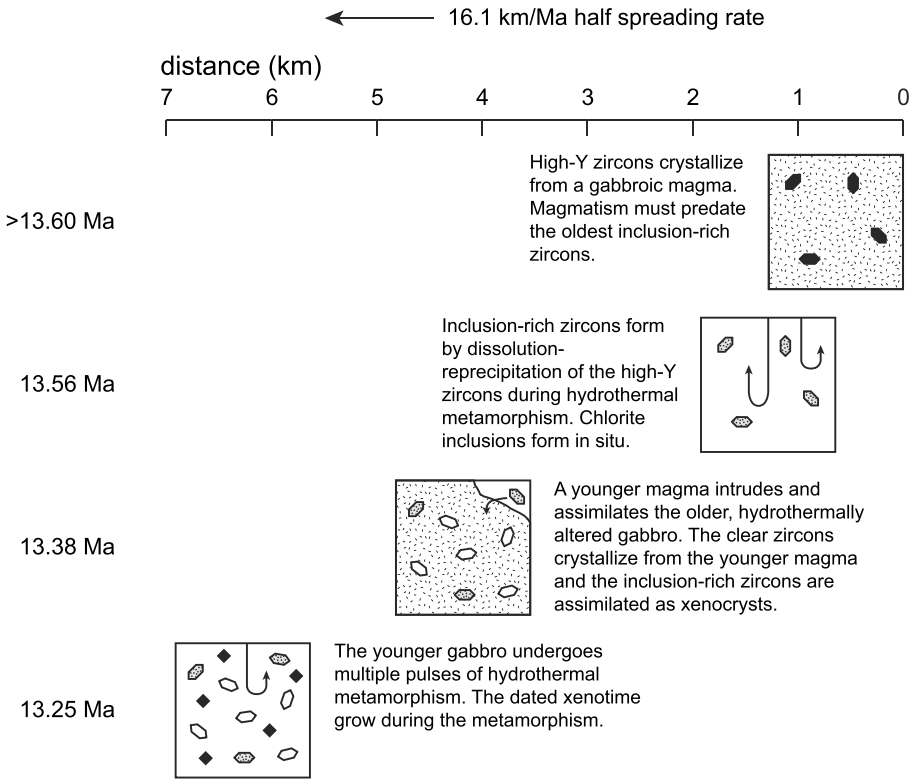

Figure 10. Model explaining the sequence of alternating magmatism and hydrothermal alteration defined by zircon and xenotime dates in the studied sample. The horizontal axis shows distance perpendicular to the ridge axis for a spreading rate of 16.1 km/Ma, and the vertical axis is date (Ma; the spacing of the dates is nonlinear). The studied sample preserves a record of two separate magmatic and hydrothermal events that occurred over a spreading distance of almost 6 km.

be less susceptible to dissolution-reprecipitation reactions than the high-Y protoliths to the inclusion-rich zircons, and as a result, the clear zircons were largely unaffected by these hydrothermal events.

The volume and composition of the magmas that the protolith to the inclusion-rich zircons crystallized from is not well constrained. Zircons in MOR settings are found in both evolved oxide bearing gabbros and more felsic plutonic compositions (i.e., quartz diorites, tonalites, and trondhjemites) [*Baines et al*., 2009; *Grimes et al*., 2009; *Grimes et al*., 2008; *Lissenberg et al*., 2009; *Rioux et al*., 2012a, 2012b, 2013; *Schwartz et al*., 2005]. For the inclusion-rich zircons, the alteration assemblage of Mg-rich chlorite, found within the zircons, suggests a mafic protolith, and other oxide gabbros from the Vema crustal section contain high-Y zircons similar to the inferred protolith for these grains [*De Hoog et al*., 2014]. However, *Jöns et al*. [2009] argued that zircon bearing chlorite-amphibole veins that cross cut serpentinized harzburgites in abyssal peridotites from the Mid-Atlantic Ridge formed by extensive hydrothermal alteration of small volume tonalitic intrusions. The small tonalitic veins may be related to hydrous gabbro melting [*Koepke et al*., 2005] or differentiation of gabbroic magmas. Whether the protolith grains to the inclusion-rich zircons crystallized from a larger gabbroic body or smaller volume tonalitic melt, the inclusion-rich zircons ultimately suggest that a gabbroic crust existed and underwent hydrothermal alteration prior to or synchronous with the dissolution-reprecipitation reactions that formed these zircons. Similarly, the metamorphic assemblage for the groundmass of sample DR10-005 is consistent with a gabbroic protolith, suggesting that the clear inclusion-free zircons most likely crystallized from a gabbroic magma. However, it is again not possible to discount the possibility that they actually formed in small evolved melt veins that cross cut the gabbro, which are now obscured by the extensive hydrothermal overprint. In this case, the thermal energy required to produce localized partial melting of hydrated gabbros would most likely come from a nearby gabbro intrusion, and the zircon dates still record the timing of local gabbroic magmatism.

The $\geq 0.218 \pm 0.016$ Ma age difference between the protolith to the inclusion-rich zircons and the youngest precisely dated clear igneous zircons (z4 and z8) implies that either the source rock for the inclusion-rich

grains was trapped at the ridge axis or the Vema crust was generated over a several kilometer-wide zone. Using the 16.1 km/Ma half-spreading rate calculated from marine magnetic anomalies [*Müller et al*., 2008], the age difference between the two zircon populations corresponds to 3.5 ± 0.3 km of spreading. Marine magnetic anomalies suggest that spreading was close to symmetrical at this time, with a spreading rate on the western side of the ridge of 16.1 km/Ma compared to a rate on the eastern side of 17.2 km/Ma [*Müller et al*., 2008]. If magmatism was roughly symmetrical on either side of the ridge, the total width of intrusive magmatism calculated using the full spreading rate of 33.3 km/Ma would be ≤7.3 km. This is a maximum estimate of the width for a 0.22 Ma age difference, because the crust might have been accreted over a distributed area, leading to displacement within the accretion zone less than the spreading rate. The chlorite inclusions in the inclusion-rich zircons suggest that the older gabbro cooled to lower amphibolite- or greenschist-facies conditions prior to intrusion of the younger magma [*Schmidt and Poli*, 1998].

Geophysical data indicate that most of the thickness of both extrusive lavas (layer 2A) and the intrusive crust is formed within the width of the inner rift valley floor at slow-spreading ridges (typically <15 km) [*Hosford et al*., 2001; *Hussenoeder et al*., 2002; *Pariso et al*., 1995; *Seher et al*., 2010]. Most ridge segments on the Mid-Atlantic Ridge have relatively narrow (<2–5 km wide) axial volcanic ridges [e.g., *Ballard and Van Andel*, 1977; *Macdonald*, 1982; *Searle*, 2013; *Searle et al*., 2010; *Smith and Cann*, 1992; *Smith et al*., 1999], suggesting focused melt delivery. The long-term temporal evolution of axial volcanic ridges and the nature of magma supply to these features are areas of ongoing research. Different studies have suggested that axial volcanic ridges may migrate within the inner rift valley floor through time [*Ballard and Van Andel*, 1977; *Barclay et al*., 1998; *Macdonald*, 1977] or represent near-steady state features [*Murton et al*., 2012; *Searle*, 2013; *Smith and Cann*, 1999]. The low melt supply and general absence of seismically imaged magma chambers at slow-spreading ridges suggest that magmatism is episodic [e.g., *Dunn and Forsyth*, 2007; *Sinton and Detrick*, 1992], and it may occur in either a single central magma chamber [*Singh et al*., 2006; *Sinha et al*., 1998; *Smith and Cann*, 1999] or numerous smaller chambers [*Nisbet and Fowler*, 1978; *Smith and Cann*, 1992]. In addition to the focused magmatism along the ridge axis, there is also evidence for much more limited off-axis volcanism, both within [*Mallows and Searle*, 2012] and outside the inner rift valley floor [*Heirtzler and Ballard*, 1977; *Macdonald*, 1982].

The data from this study constrain the temporal evolution of intrusive magmatism during formation of the crust. The ≥0.22 Ma of magmatism recorded in the studied sample could reflect either lateral migration of a focused zone of intrusive magmatism through time or progressive formation of the lower crust through episodic pulses of distributed magmatism within the axial valley. *Macdonald* [1982] suggested that the focus of magmatism at slow-spreading ridges may migrate as a result of the episodic nature of magmatism; if the crust cools between magmatic pulses, preexisting zones of weakness exploited by previous magmatism may strengthen and the next magmatic pulse may follow a different path. The Vema crust is adjacent to a major transform fault, where the crust is relatively cool and there is a decreased magma supply [*Bender et al*., 1984; *Langmuir and Bender*, 1984], as evident from the thin crust. This tectonic setting is particularly prone to cooling between magmatic pulses and the chlorite inclusions in the inclusion-rich zircons provide evidence for hydrothermal circulation and cooling between the magmatic pulses in the studied sample.

The implied width of the magmatic zone from the U-Pb dates may also reflect interaction between the MAR and the Vema transform. At ridge-transform intersections on slow-spreading ridges, the neovolcanic zones can become discontinuous, widen, and bend into the transform [*Fox and Gallo*, 1984; *Macdonald et al*., 1986; *Sempéré et al*., 1993; *Smith et al*., 1999]. At the current ridge-transform intersection on the eastern side of the Vema transform, the ridge axis is offset ~4 km to the west [*Macdonald et al*., 1986]. Modeling suggests that the deviation of the ridge axis depends on the relative contributions of tensile stress at the ridge and shear stress from the transform [*Neves et al*., 2004; *Phipps Morgan and Parmentier*, 1984]: e.g., if the transform fault is locked, the resultant stress field causes the ridge axis to rotate toward the transform. The stress field at ridge-transform intersections may change through time depending of the degree of coupling across the transform [*Fox and Gallo*, 1984], which may in turn be linked to changes in lithosphere thickness associated with episodic magmatism [*Macdonald et al*., 1986]; periods of high magma supply may lead to a thinner lithosphere, decreased coupling across the transform, and minimal rotation of the ridge axis, whereas periods of low magma supply may lead to a thicker lithosphere, increased coupling, and larger deviations of the ridge axis. Such variations in the stress field may explain the mutual overprinting of ridge parallel and oblique normal faults at ridge-transform intersections [*Fox and Gallo*, 1984; *Macdonald et al*., 1986]. The locus of magma intrusion will

also follow the local stress field, and episodic changes in the stress field could lead to lateral (east-west at Vema) variations in the location of the axial magma chamber, producing a several kilometer-wide zone of magmatism during crustal accretion.

A third possible explanation of the U-Pb data is that the observed age difference between the inclusion-rich and clear zircons reflects different intrusion depths of the parental gabbros, rather than lateral migration of the locus of magmatism. Geochemical data, geophysical data, and exposed mantle lithosphere suggests that a significant volume of gabbro may crystallize in the mantle below slow-spreading ridges [*Cannat*, 1993, 1996; *Cannat et al*., 1997; *Coogan et al*., 2001a; *Kelemen et al*., 2002; *Lizarralde et al*., 2004], and some slow-spreading crust is a mixture of peridotite and gabbro [*Cannat*, 1993, 1996; *Dick et al*., 2008]. At Atlantis Bank (SWIR), *Schwartz et al*. [2005] suggested that plutonic rocks from the lower crust with anomalously old U-Pb dates, relative to predicted ages based on marine magnetic anomalies, could have crystallized 5–18 km below the moho and then have been subsequently incorporated into the crust. The ≥0.22 Ma age difference between the two zircon populations in this study would require that the older gabbroic magma crystallized and underwent hydrothermal alteration ≥3.5 km below the base of the crust. This hydrothermally altered gabbro would have then had to move vertically to crustal levels and be partially assimilated by a younger magma. It is not possible to discount this model; however, we suggest that lateral migration of the locus of magmatism provides a more plausible explanation of the data for the Vema crust.

In either of the first two models, the ≥0.22 Ma age difference documented in this study suggests that either a focused zone of intrusive magmatism at ridge-transform intersections, and potentially at slow-spreading ridges in general, migrates several kilometers normal to the ridge on timescales of tens to hundreds of thousands of years or intrusive magmatism is distributed over several kilometers across the axis. If the observations from this study reflect general processes, they predict that there will not be a simple linear relationship between the age of the intrusive crust and distance from the ridge axis. This hypothesis could be tested by further high-precision dating of closely spaced samples from oceanic transforms. The age-versus-distance relationship for the full data set of Vema gabbros we have studied permits a distributed zone of axial magmatism—for example, there is an offset of 0.08 ± 0.04 Ma between the youngest dates in DR10-005 and DR10-007, which were both recovered from a single dredge [*Lissenberg et al*., 2009; *Rioux et al*., 2012b]—however, a larger data set of precisely located samples is needed.

A key result from our previous research on Vema gabbros was that most of the studied samples contained a range of zircons dates [*Lissenberg et al*., 2009; *Rioux et al*., 2012b]. We attributed the intrasample variability in $^{206}Pb/^{238}U$ dates to either protracted magma crystallization or assimilation of older zircon from adjacent wall rocks. The results of this study provide strong evidence for the latter: assimilation during igneous crystallization. The evidence for assimilation of hydrothermally altered crust by later gabbroic magmatism contrasts with prior research on the Cl content of ridge plutonic and volcanic rocks [*Coogan*, 2003; *Coogan et al*., 2003; *Michael and Cornell*, 1998; *Michael and Schilling*, 1989]. Elevated Cl contents in plutonic and volcanic whole rocks and amphibole suggest that magmas at fast-spreading ridges assimilate a significant volume of hydrothermally altered crust [*Coogan*, 2003; *Coogan et al*., 2003; *Michael and Cornell*, 1998; *Michael and Schilling*, 1989]. However, similar Cl enrichments have not been observed at slow-spreading ridges, and the inferred absence of assimilation has been attributed to lower magma fluxes and deeper crystallization below areas of significant hydrothermal metamorphism [*Coogan*, 2003; *Michael and Cornell*, 1998; *Michael and Schilling*, 1989]. The results from this study show that assimilation of hydrothermally altered crust may be an important processes at slow-spreading ridges, although it may be restricted to the ends of ridge segments, where variable stress fields lead to a wider magmatic zone and the thin crust allows hydrothermal systems to access the lower crust.

5. Conclusions

Multiple U-bearing trace minerals from a hydrothermally altered gabbro from the Vema lithospheric section on the Mid-Atlantic Ridge record the timing of, and interaction between, hydrothermal metamorphism and magmatism during formation of the lower oceanic crust. The oldest zircon population contains ubiquitous chlorite inclusions and has very low Th/U (0.05–0.09). Th-corrected $^{206}Pb/^{238}U$ dates from these zircons range from 13.598 ± 0.012 to 13.503 ± 0.018 Ma. The zircon textures and mineral inclusions suggest that these grains formed by dissolution-reprecipitation of older igneous zircons during or following a hydrothermal

metamorphic event. A second population of previously dated clear inclusion-free igneous zircons with sector zoning record younger Th-corrected $^{206}Pb/^{238}U$ dates of 13.53 ± 0.10 to 13.353 ± 0.057 Ma [*Lissenberg et al.*, 2009; *Rioux et al.*, 2012b]. Ti concentrations (5.1–12.0 ppm), measured in this study, moderate Th/U (0.31–0.39), and CL zoning patterns are all consistent with an igneous origin for these zircons. The simplest explanation of the two zircon populations is that the older inclusion-rich zircons represent xenocrysts from an older hydrothermally altered gabbro that were assimilated into a younger gabbroic magma, from which the clear zircons crystallized. Thermodynamic calculations suggest that the inclusion-rich zircons could have survived chlorite breakdown during assimilation. Xenotimes from the sample, which textural evidence suggests grew during subsequent hydrothermal alteration of the younger gabbro, record maximum $^{206}Pb/^{238}U$ dates of 13.34 ± 0.16 to 12.993 ± 0.055 Ma. Taken together, the U-Pb dates record evidence of two separate hydrothermal and magmatic events during accretion of the lower crust.

The mineral assemblage of the studied sample records evidence of protracted metamorphism during the final hydrothermal event. The earliest evidence for hydrothermal overprinting of the magmatic mineral assemblage is cummingtonitic amphibole that formed at comparatively high temperatures (~600–950°C). This was followed by two major stages of lower temperature fluid-rock interaction. The first of these stages was localized fluid flow at temperatures of ~200–400°C, leading to kerolite formation in veins. Subsequent diffuse fluid flow at slightly lower temperatures (~150–200°C) caused widespread formation of prehnite + chlorite.

The age difference between the older zircon xenocrysts and the younger igneous zircons constrains the width of the magmatic zone during lower crustal accretion. The 0.22 Ma age difference corresponds to 3.5 km of spreading. We attribute the distributed magmatism to east–west migration of the axial magmatic zone or to distributed magmatism over several kilometers across the ridge axis, related to either the episodic nature of magmatism at slow-spreading ridges and/or episodic changes in the local stress field at the ridge-transform intersection. The evidence for assimilation of older hydrothermally altered crust into younger gabbroic magmas contrasts with previous studies of the Cl content of mid-ocean ridge gabbros and basalts and suggests that this process is locally important at slow-spreading ridges. The results of this study show the power of using high-precision U-Pb geochronology to determine the timing of magmatic and hydrothermal processes at mid-ocean ridge spreading centers.

Acknowledgments

This research was partially funded by National Science Foundation grants OCE-0727914 (S.B.), OCE-0960892 (S.B.), and EAR-1250522 (M.R.) and Natural Environment Research Council grant NE/H020004/1 (J.L.). N.J. and W.B. acknowledge support through DFG research center/excellence cluster "The Ocean in the Earth System." We thank J. Creveling for doing the zircon separations, M. Krawczynski for his help making serial sections of the studied sample, L. Harrison for assistance with ArcMap, N. Chatterjee for assistance with the electron microprobe at MIT, G. Seward for assistance with the scanning electron microscope at UCSB, B. Mader and P. Appel for assistance with the electron microprobe at the University of Kiel, T. Grove for helpful discussions of chlorite-breakdown reactions, and D. Wilson for useful discussions of MOR processes. All of the data relevant to this research has been included in the tables and supporting information tables associated with this paper or in the papers cited within.

References

Anczkiewicz, R., F. Oberli, J. P. Burg, I. M. Villa, D. Günther, and M. Meier (2001), Timing of normal faulting along the Indus Suture in Pakistan Himalaya and a case of major $^{231}Pa/^{235}U$ initial disequilibrium in zircon, *Earth Planet. Sci. Lett.*, *191*, 101–114.

Andersen, M. B., C. H. Stirling, B. Zimmermann, and A. N. Halliday (2010), Precise determination of the open ocean $^{234}U/^{238}U$ composition, *Geochem. Geophys. Geosyst.*, *11*, Q12003, doi:10.1029/2010GC003318.

Auzende, J. M., D. Bideau, E. Bonatti, M. Cannat, J. Honnorez, Y. Lagabrielle, J. Malavieille, V. Mamaloukas-Frangoulis, and C. Mevel (1989), Direct observation of a section through slow-spreading oceanic crust, *Nature*, *337*, 726–729.

Bach, W., J. C. Alt, Y. Niu, S. E. Humphris, J. Erzinger, and H. J. B. Dick (2001), The geochemical consequences of late-stage low-grade alteration of lower ocean crust at the SW Indian Ridge: Results from ODP Hole 735B (Leg 176), *Geochim. Cosmochim. Acta*, *65*, 3267–3287.

Bach, W., B. Peucker-Ehrenbrink, S. R. Hart, and J. S. Blusztajn (2003), Geochemistry of hydrothermally altered oceanic crust: DSDP/ODP Hole 504B—Implications for seawater-crust exchange budgets and Sr- and Pb-isotopic evolution of the mantle, *Geochem. Geophys. Geosyst.*, *4*(3), 8904, doi:10.1029/2002GC000419.

Bacon, C. R., T. W. Sisson, and F. K. Mazdab (2007), Young cumulate complex beneath Veniaminof caldera, Aleutian arc, dated by zircon in erupted plutonic blocks, *Geology*, *35*, 491–494.

Baines, A. G., M. J. Cheadle, B. E. John, C. B. Grimes, J. J. Schwartz, and J. L. Wooden (2009), SHRIMP Pb/U zircon ages constrain gabbroic crustal accretion at Atlantis Bank on the ultraslow-spreading Southwest Indian Ridge, *Earth Planet. Sci. Lett.*, *287*, 540–550.

Ballard, R. D., and T. H. Van Andel (1977), Morphology and tectonics of the inner rift valley at lat 36°50′N on the Mid-Atlantic Ridge, *Geol. Soc. Am. Bull.*, *88*, 507–530.

Barboni, M., and B. Schoene (2014), Short eruption window revealed by absolute crystal growth rates in a granitic magma, *Nat. Geosci.*, *7*, 524–528.

Barclay, A. H., D. R. Toomey, and S. C. Solomon (1998), Seismic structure and crustal magmatism at the Mid-Atlantic Ridge, 35°N, *J. Geophys. Res.*, *103*, 17,827–17,844, doi:10.1029/98JB01275.

Bazylev, B., S. Silantiev, H. Dick, and N. Kononkova (2001), Magmatic amphiboles and micas in oceanic peridotites and some specific features of the related magmas: 15°20′N MAR fracture zone, *Russ. J. Earth Sci.*, *3*, 219–234.

Beard, J. S., B. R. Frost, P. Fryer, A. McCaig, R. Searle, B. Ildefonse, P. Zinin, and S. K. Sharma (2009), Onset and progression of serpentinization and magnetite formation in olivine-rich troctolite from IODP Hole U1309D, *J. Petrol.*, *50*, 387–403.

Bender, J. F., C. H. Langmuir, and G. N. Hanson (1984), Petrogenesis of basalt glasses from the Tamayo region, East Pacific Rise, *J. Petrol.*, *25*, 213–254.

Bindeman, I., A. Schmitt, and J. Valley (2006), U–Pb zircon geochronology of silicic tuffs from the Timber Mountain/Oasis Valley caldera complex, Nevada: Rapid generation of large volume magmas by shallow-level remelting, *Contrib. Mineral. Petrol.*, *152*, 649–665.

Blackman, D. K., B. Ildefonse, B. E. John, Y. Ohara, D. J. Miller, C. J. MacLeod, and the Expedition 304/305 Scientists (2006), Expedition 304/305 summary, in *Proceedings of the Integrated Ocean Drilling Program*, vol. 304/305, pp. 1–60, Integrated Ocean Drilling Program Management International, Inc., College Station, Tex.

Blundy, J., and B. Wood (2003), Mineral-melt partitioning of uranium, thorium and their daughters, *Rev. Mineral. Geochem.*, *52*, 59–123.

Bonatti, E., J. Honnorez, P. Kirst, and F. Radicati (1975), Metagabbros from the Mid-Atlantic Ridge at 06°N: Contact-hydrothermal-dynamic metamorphism beneath the axial valley, *J. Geol.*, *83*, 61–78.
Bonatti, E., M. Ligi, D. Brunelli, A. Cipriani, P. Fabretti, V. Ferrante, L. Gasperini, and L. Ottolini (2003), Mantle thermal pulses below the Mid-Atlantic Ridge and temporal variations in the formation of oceanic lithosphere, *Nature*, *423*, 499–505.
Bonatti, E., D. Brunelli, W. R. Buck, A. Cipriani, P. Fabretti, V. Ferrante, L. Gasperini, and M. Ligi (2005), Flexural uplift of a lithospheric slab near the Vema transform (Central Atlantic): Timing and mechanisms, *Earth Planet. Sci. Lett.*, *240*, 642–655.
Bowring, J. F., N. M. McLean, and S. A. Bowring (2011), Engineering cyber infrastructure for U-Pb geochronology: Tripoli and U-Pb_Redux, *Geochem. Geophys. Geosyst.*, *12*, Q0AA19, doi:10.1029/2010GC003479.
Brindley, G., D. L. Bish, and H.-M. Wan (1977), The nature of kerolite, its relation to talc and stevensite, *Mineral. Mag.*, *41*, 443–452.
Brindley, G., D. Bish, and H.-M. Wan (1979), Compositions, structures, and properties of nickel-containing minerals in the kerolite-pimelite series, *Am. Mineral.*, *64*, 615–625.
Brunelli, D., M. Seyler, A. Cipriani, L. Ottolini, and E. Bonatti (2006), Discontinuous melt extraction and weak refertilization of mantle peridotites at the Vema lithospheric section (Mid-Atlantic Ridge), *J. Petrol.*, *47*, 745–771.
Burnham, A. D., and A. J. Berry (2012), An experimental study of trace element partitioning between zircon and melt as a function of oxygen fugacity, *Geochim. Cosmochim. Acta*, *95*, 196–212.
Cannat, M. (1993), Emplacement of mantle rocks in the seafloor at mid-ocean ridges, *J. Geophys. Res.*, *98*, 4163–4172, doi:10.1029/92JB02221.
Cannat, M. (1996), How thick is the magmatic crust at slow spreading oceanic ridges?, *J. Geophys. Res.*, *101*, 2847–2857, doi:10.1029/95JB03116.
Cannat, M., F. Chatin, H. Whitechurch, and G. Ceuleneer (1997), Gabbroic rocks trapped in the upper mantle at the Mid-Atlantic Ridge, in *Proceedings of the Ocean Drilling Program*, Sci. Results, pp. 243–264, Ocean Drilling Program, College Station, Tex.
Chen, J. H., R. Lawrence Edwards, and G. J. Wasserburg (1986a), ^{238}U, ^{234}U and ^{232}Th in seawater, *Earth Planet. Sci. Lett.*, *80*, 241–251.
Chen, J. H., G. J. Wasserburg, K. L. von Damm, and J. M. Edmond (1986b), The U-Th-Pb systematics in hot springs on the East Pacific Rise at 21°N and Guaymas Basin, *Geochim. Cosmochim. Acta*, *50*, 2467–2479.
Cheng, H., R. L. Edwards, J. Hoff, C. D. Gallup, D. A. Richards, and Y. Asmerom (2000), The half-lives of uranium-234 and thorium-230, *Chem. Geol.*, *169*, 17–33.
Cherniak, D. J., and E. B. Watson (2000), Pb diffusion in zircon, *Chem. Geol.*, *172*, 5–24.
Cherniak, D. J., J. M. Hanchar, and E. B. Watson (1997), Rare-earth diffusion in zircon, *Chem. Geol.*, *134*, 289–301.
Chernosky, J. V. (1974), The upper stability of clinochlore at low pressure and the free energy of formation of Mg-Cordierite, *Am. Mineral.*, *59*, 496–507.
Chernosky, J. V., R. G. Berman, and L. T. Bryndzia (1988), Stability, phase relations, and thermodynamic properties of chlorite and serpentine group minerals, *Rev. Mineral. Geochem.*, *19*, 295–346.
Coogan, L. A. (2003), Contaminating the lower crust in the Oman ophiolite, *Geology*, *31*, 1065–1068.
Coogan, L. A., C. J. MacLeod, H. J. B. Dick, S. J. Edwards, A. Kvassnes, J. H. Natland, P. T. Robinson, G. Thompson, and M. J. O'Hara (2001a), Whole-rock geochemistry of gabbros from the Southwest Indian Ridge: Constraints on geochemical fractionations between the upper and lower oceanic crust and magma chamber processes at (very) slow-spreading ridges, *Chem. Geol.*, *178*, 1–22.
Coogan, L. A., R. N. Wilson, K. M. Gillis, and C. J. MacLeod (2001b), Near-solidus evolution of oceanic gabbros: Insights from amphibole geochemistry, *Geochim. Cosmochim. Acta*, *65*, 4339–4357.
Coogan, L. A., N. C. Mitchell, and M. J. O'Hara (2003), Roof assimilation at fast spreading ridges: An investigation combining geophysical, geochemical, and field evidence, *J. Geophys. Res.*, *108*(B1), 2002, doi:10.1029/2001JB001171.
Coogan, L. A., K. A. Howard, K. M. Gillis, M. J. Bickle, H. Chapman, A. J. Boyce, G. R. T. Jenkin, and R. N. Wilson (2006), Chemical and thermal constraints on focussed fluid flow in the lower oceanic crust, *Am. J. Sci.*, *306*, 389–427.
Coombs, D. S., A. J. Ellis, W. S. Fyfe, and A. M. Taylor (1959), The zeolite facies, with comments on the interpretation of hydrothermal syntheses, *Geochim. Cosmochim. Acta*, *17*, 53–107.
De Hoog, J. C. M., C. J. Lissenberg, R. A. Brooker, R. Hinton, D. Trail, and E. Hellebrand (2014), Hydrogen incorporation and charge balance in natural zircon, *Geochim. Cosmochim. Acta*, *141*, 472–486.
Dekov, V. M., J. Cuadros, W. C. Shanks, and R. A. Koski (2008b), Deposition of talc—kerolite-smectite—smectite at seafloor hydrothermal vent fields: Evidence from mineralogical, geochemical and oxygen isotope studies, *Chem. Geol.*, *247*, 171–194.
Dekov, V., J. Scholten, C.-D. Garbe-Schönberg, R. Botz, J. Cuadros, M. Schmidt, and P. Stoffers (2008a), Hydrothermal sediment alteration at a seafloor vent field: Grimsey Graben, Tjörnes Fracture Zone, north of Iceland, *J. Geophys. Res.*, *113*, B11101, doi:10.1029/2007JB005526.
Delacour, A., G. L. Früh-Green, and S. M. Bernasconi (2008), Sulfur mineralogy and geochemistry of serpentinites and gabbros of the Atlantis Massif (IODP Site U1309), *Geochim. Cosmochim. Acta*, *72*, 5111–5127.
Delanghe, D., E. Bard, and B. Hamelin (2002), New TIMS constraints on the uranium-238 and uranium-234 in seawaters from the main ocean basins and the Mediterranean Sea, *Mar. Chem.*, *80*, 79–93.
DeRudder, R. D., and C. W. Beck (1963), Stevensite and talc—Hydrothermal alteration products of wollastonite, *Clays Clay Miner.*, *11*, 188–199.
Dick, H. J. B., M. A. Tivey, and B. E. Tucholke (2008), Plutonic foundation of a slow-spreading ridge segment: Oceanic core complex at Kane Megamullion, 23°30′N, 45°20′W, *Geochem. Geophys. Geosyst.*, *9*, Q05014, doi:10.1029/2007GC001645.
Dunn, R. A., and D. W. Forsyth (2007), 1.12—Crust and lithospheric structure—Seismic structure of mid-ocean ridges, in *Treatise on Geophysics*, edited by G. Schubert, pp. 419–443, Elsevier, Amsterdam.
Dutta, R., and N. Mandal (2012), Effects of pressure on the elasticity and stability of zircon ($ZrSiO_4$): First-principle investigations, *Comput. Mater. Sci.*, *54*, 157–164.
Eberl, D. D., B. F. Jones, and H. N. Khoury (1982), Mixed-layer kerolite/stevensite from the Amargosa Desert, Nevada, *Clays Clay Miner.*, *30*, 321.
Ferry, J., and E. Watson (2007), New thermodynamic models and revised calibrations for the Ti-in-zircon and Zr-in-rutile thermometers, *Contrib. Mineral. Petrol.*, *154*, 429–437.
Fletcher, J. M., C. J. Stephens, E. U. Petersen, and L. Skerl (1997), Greenschist facies hydrothermal alteration of oceanic gabbros: A case study of element mobility and reaction paths, in *Proceedings of the Ocean Drilling Program*, *Sci. Results*, pp. 389–398, Ocean Drilling Program, College Station, Tex.
Fox, P. J., and D. G. Gallo (1984), A tectonic model for ridge-transform-ridge plate boundaries: Implications for the structure of oceanic lithosphere, *Tectonophysics*, *104*, 205–242.
Frey, M., C. D. Capitani, and J. G. Liou (1991), A new petrogenetic grid for low-grade metabasites, *J. Metamorph. Geol.*, *9*, 497–509.
Frost, B. R., J. S. Beard, A. McCaig, and E. Condliffe (2008), The formation of micro-rodingites from IODP Hole U1309D: Key to understanding the process of serpentinization, *J. Petrol.*, *49*, 1579–1588.
Fu, B., F. Page, A. Cavosie, J. Fournelle, N. Kita, J. Lackey, S. Wilde, and J. Valley (2008), Ti-in-zircon thermometry: Applications and limitations, *Contrib. Mineral. Petrol.*, *156*, 197–215.

Geisler, T., U. Schaltegger, and F. Tomaschek (2007), Re-equilibration of zircon in aqueous fluids and melts, *Elements*, *3*, 43–50.
Gillis, K. M., G. Thompson, and D. S. Kelley (1993), A view of the lower crustal component of hydrothermal systems at the Mid-Atlantic Ridge, *J. Geophys. Res.*, *98*, 19,597–19,619, doi:10.1029/93JB01717.
Grimes, C. B., B. E. John, M. J. Cheadle, and J. L. Wooden (2008), Protracted construction of gabbroic crust at a slow spreading ridge: Constraints from $^{206}Pb/^{238}U$ zircon ages from Atlantis Massif and IODP Hole U1309D (30°N, MAR), *Geochem. Geophys. Geosyst.*, *9*, doi:10.1029/2008GC002063.
Grimes, C., B. John, M. Cheadle, F. Mazdab, J. Wooden, S. Swapp, and J. Schwartz (2009), On the occurrence, trace element geochemistry, and crystallization history of zircon from in situ ocean lithosphere, *Contrib. Mineral. Petrol.*, *158*, 757–783.
Guiraud, M., and R. Powell (2006), P–V–T relationships and mineral equilibria in inclusions in minerals, *Earth Planet. Sci. Lett.*, *244*, 683–694.
Hacker, B. R., and G. A. Abers (2004), Subduction Factory 3: An Excel worksheet and macro for calculating the densities, seismic wave speeds, and H_2O contents of minerals and rocks at pressure and temperature, *Geochem. Geophys. Geosyst.*, *5*, Q01005, doi:10.1029/2003GC000614.
Hacker, B. R., G. A. Abers, and S. M. Peacock (2003), Subduction factory: 1. Theoretical mineralogy, densities, seismic wave speeds, and H_2O contents, *J. Geophys. Res.*, *108*(B1), 2029, doi:10.1029/2001JB001127.
Heezen, B. C., R. D. Gerard, and M. Tharp (1964), The Vema fracture zone in the equatorial Atlantic, *J. Geophys. Res.*, *69*, 733–739, doi:10.1029/JZ069i004p00733.
Heirtzler, J., and R. Ballard (1977), Submersible observations at the Hole 332B area, *Initial Rep. Deep Sea Drill. Proj.*, *37*, 363–366.
Hiess, J., D. J. Condon, N. McLean, and S. R. Noble (2012), $^{238}U/^{235}U$ systematics in terrestrial Uranium-bearing minerals, *Science*, *335*, 1610–1614.
Holland, T. J. B., and R. Powell (1998), An internally consistent thermodynamic data set for phases of petrological interest, *J. Metamorph. Geol.*, *16*, 309–343.
Holland, T. J. B., and R. Powell (2011), An improved and extended internally consistent thermodynamic dataset for phases of petrological interest, involving a new equation of state for solids, *J. Metamorph. Geol.*, *29*, 333–383.
Honnorez, J., C. Mével, and R. Montigny (1984), Geotectonic significance of gneissic amphibolites from the Vema fracture zone, equatorial Mid-Atlantic Ridge, *J. Geophys. Res.*, *89*, 11,379–11,400, doi:10.1029/JB089iB13p11379.
Hosford, A., J. Lin, and R. S. Detrick (2001), Crustal evolution over the last 2 m.y. at the Mid-Atlantic Ridge OH-1 segment, 35°N, *J. Geophys. Res.*, *106*, 13,269–13,285, doi:10.1029/2001JB000235.
Hoskin, P. W. O. (2005), Trace-element composition of hydrothermal zircon and the alteration of Hadean zircon from the Jack Hills, Australia, *Geochim. Cosmochim. Acta*, *69*, 637–648.
Hoskin, P. W. O., and L. P. Black (2000), Metamorphic zircon formation by solid-state recrystallization of protolith igneous zircon, *J. Metamorph. Geol.*, *18*, 423–439.
Hussenoeder, S. A., G. M. Kent, and R. S. Detrick (2002), Upper crustal seismic structure of the slow spreading Mid-Atlantic Ridge, 35°N: Constraints on volcanic emplacement processes, *J. Geophys. Res.*, *107*(B8), 2156, doi:10.1029/2001JB001691.
Ito, E., and A. T. Anderson Jr. (1983), Submarine metamorphism of gabbros from the Mid-Cayman Rise: Petrographic and mineralogic constraints on hydrothermal processes at slow-spreading ridges, *Contrib. Mineral. Petrol.*, *82*, 371–388.
Jaffey, A. H., K. F. Flynn, L. E. Glendenin, W. C. Bentley, and A. M. Essling (1971), Precision measurement of half-lives and specific activities of ^{235}U and ^{238}U, *Phys. Rev. C*, *4*, 1889–1906.
Jarosewich, E., and L. A. Boatner (1991), Rare-earth element reference samples for electron microprobe analysis, *Geostand. Newsl.*, *15*, 397–399.
Jenkins, D. M., and J. V. Chernosky (1986), Phase equilibria and crystallochemical properties of Mg-chlorite, *Am. Mineral.*, *71*, 924–936.
John, B. E., M. J. Cheadle, M. Rioux, J. L. Wooden, and A. G. Baines (2012), Textures and geochemistry of zircons in ODP holes 735B and 1105A, Atlantis Bank, SWIR AGU Fall Meeting, San Francisco, Calif.
Jöns, N., W. Bach, and T. Schroeder (2009), Formation and alteration of plagiogranites in an ultramafic-hosted detachment fault at the Mid-Atlantic Ridge (ODP Leg 209), *Contrib. Mineral. Petrol.*, *157*, 625–639.
Kastens, K., E. Bonatti, D. Caress, G. Carrara, O. Dauteuil, G. Frueh-Green, M. Ligi, and P. Tartarotti (1998), The Vema Transverse Ridge (Central Atlantic), *Mar. Geophys. Res.*, *20*, 533–556.
Kelemen, P. B., E. Kikawa, D. J. Miller, and S. S. Party (2002), Leg 209 summary: Processes in a 20-km-thick conductive boundary layer beneath the Mid-Atlantic Ridge, 14–16 N, in *Proceedings of the Ocean Drilling Program*, *Sci. Results*, pp. 1–33, Ocean Drilling Program, College Station, Tex.
Koepke, J., S. T. Feig, and J. Snow (2005), Hydrous partial melting within the lower oceanic crust, *Terra Nova*, *17*, 286–291.
Kong, L. S. L., S. C. Solomon, and G. M. Purdy (1992), Microearthquake characteristics of a mid-ocean ridge along-axis high, *J. Geophys. Res.*, *97*, 1659–1685, doi:10.1029/91JB02566.
Langmuir, C. H., and J. F. Bender (1984), The geochemistry of oceanic basalts in the vicinity of transform faults: Observations and implications, *Earth Planet. Sci. Lett.*, *69*, 107–127.
Lede, J., F. Lapicque, J. Villermaux, B. Cales, A. Ounalli, J. F. Baumard, and A. M. Anthony (1982), Production of hydrogen by direct thermal decomposition of water: Preliminary investigations, *Int. J. Hydrogen Energy*, *7*, 939–950.
Liou, J. (1971), Synthesis and stability relations of prehnite, $Ca_2Al_2Si_3O_{10}(OH)_2$, *Am. Mineral.*, *56*, 507–531.
Lissenberg, C. J., M. Rioux, N. Shimizu, S. A. Bowring, and C. Mevel (2009), Zircon dating of oceanic crustal accretion, *Science*, *323*, 1048–1050.
Lizarralde, D., J. B. Gaherty, J. A. Collins, G. Hirth, and S. D. Kim (2004), Spreading-rate dependence of melt extraction at mid-ocean ridges from mantle seismic refraction data, *Nature*, *432*, 744–747.
Ludwig, K. A., C.-C. Shen, D. S. Kelley, H. Cheng, and R. L. Edwards (2011), U–Th systematics and ^{230}Th ages of carbonate chimneys at the Lost City Hydrothermal Field, *Geochim. Cosmochim. Acta*, *75*, 1869–1888.
Macdonald, K. C. (1977), Near-bottom magnetic anomalies, asymmetric spreading, oblique spreading, and tectonics of the Mid-Atlantic Ridge near lat 37°N, *Geol. Soc. Am. Bull.*, *88*, 541–555.
Macdonald, K. C. (1982), Mid-ocean ridges: Fine scale tectonic, volcanic and hydrothermal processes within the plate boundary zone, *Annu. Rev. Earth Planet. Sci.*, *10*, 155–190.
Macdonald, K. C., D. A. Castillo, S. P. Miller, P. J. Fox, K. A. Kastens, and E. Bonatti (1986), Deep-tow studies of the Vema Fracture Zone: 1. Tectonics of a major slow slipping transform fault and its intersection with the Mid-Atlantic Ridge, *J. Geophys. Res.*, *91*, 3334–3354, doi:10.1029/JB091iB03p03334.
Mallows, C., and R. C. Searle (2012), A geophysical study of oceanic core complexes and surrounding terrain, Mid-Atlantic Ridge 13°N–14°N, *Geochem. Geophys. Geosyst.*, *13*, Q0AG08, doi:10.1029/2012GC004075.
Mattinson, J. M. (1973), Anomalous isotopic composition of lead in young zircons, in *Carnegie Institution of Washington Yearbook*, vol. 72, pp. 613–616, Carnegie Institution, Washington D. C.

Mattinson, J. M. (2005), Zircon U/Pb chemical abrasion (CA-TIMS) method; combined annealing and multi-step partial dissolution analysis for improved precision and accuracy of zircon ages, *Chem. Geol.*, *220*, 47–66.
McLean, N. M., J. F. Bowring, and S. A. Bowring (2011), An algorithm for U-Pb isotope dilution data reduction and uncertainty propagation, *Geochem. Geophys. Geosyst.*, *12*, Q0AA18, doi:10.1029/2010GC003478.
Mevel, C. (1988), Metamorphism in oceanic layer 3, Gorringe Bank, eastern Atlantic, *Contrib. Mineral. Petrol.*, *100*, 496–509.
Michael, P. J., and J.-G. Schilling (1989), Chlorine in mid-ocean ridge magmas: Evidence for assimilation of seawater-influenced components, *Geochim. Cosmochim. Acta*, *53*, 3131–3143.
Michael, P. J., and W. C. Cornell (1998), Influence of spreading rate and magma supply on crystallization and assimilation beneath mid-ocean ridges: Evidence from chlorine and major element chemistry of mid-ocean ridge basalts, *J. Geophys. Res.*, *103*, 18,325–18,356, doi:10.1029/98JB00791.
Michard, A., and F. Albarede (1985), Hydrothermal uranium uptake at ridge crests, *Nature*, *317*, 244–246.
Miyashiro, A., F. Shido, and M. Ewing (1971), Metamorphism in the Mid-Atlantic Ridge near 24 degrees and 30 degrees N, *Philos. Trans. R. Soc. London, Ser. A: Math. Phys. Sci.*, *268*, 589–603.
Müller, R. D., M. Sdrolias, C. Gaina, and W. R. Roest (2008), Age, spreading rates, and spreading asymmetry of the world's ocean crust, *Geochem. Geophys. Geosyst.*, *9*, Q04006, doi:10.1029/2007GC001743.
Murton, B., N. Schroth, T. LeBas, P. Van Calsteren, I. Yeo, K. Achenbach, and R. Searle (2012), Slow-spreading oceanic crust formed by steady-state axial volcanic ridges AGU Fall Meeting, pp. 1723.
Neves, M. C., M. H. P. Bott, and R. C. Searle (2004), Patterns of stress at midocean ridges and their offsets due to seafloor subsidence, *Tectonophysics*, *386*, 223–242.
Nisbet, E. G., and C. M. R. Fowler (1978), The Mid-Atlantic Ridge at 37 and 45° N: Some geophysical and petrological constraints, *Geophys. J. Int.*, *54*, 631–660.
Nozaka, T., and P. Fryer (2011), Alteration of the oceanic lower crust at a slow-spreading axis: Insight from vein-related zoned halos in olivine gabbro from Atlantis Massif, Mid-Atlantic Ridge, *J. Petrol.*, *52*, 643–664.
Nozaka, T., P. Fryer, and M. Andreani (2008), Formation of clay minerals and exhumation of lower-crustal rocks at Atlantis Massif, Mid-Atlantic Ridge, *Geochem. Geophys. Geosyst.*, *9*, Q11005, doi:10.1029/2008GC002207.
Özkan, H., and J. C. Jamieson (1978), Pressure dependence of the elastic constants of nonmetamict zircon, *Phys. Chem. Miner.*, *2*, 215–224.
Pariso, J. E., J.-C. Sempéré, and C. Rommevaux (1995), Temporal and spatial variations in crustal accretion along the Mid-Atlantic Ridge (29°–31° 30'N) over the last 10 m.y.: Implications from a three-dimensional gravity study, *J. Geophys. Res.*, *100*, 17,781–17,794, doi:10.1029/95JB01146.
Parkinson, C. D., and I. Katayama (1999), Present-day ultrahigh-pressure conditions of coesite inclusions in zircon and garnet: Evidence from laser Raman microspectroscopy, *Geology*, *27*, 979–982.
Parrish, R. R., R. R. Parrish, and S. R. Noble (2003), Zircon U-Th-Pb geochronology by isotope dilution-thermal ionization mass spectrometry (ID-TIMS), *Rev. Mineral. Geochem.*, *53*, 183–213.
Phipps Morgan, J., and E. M. Parmentier (1984), Lithospheric stress near a ridge-transform intersection, *Geophys. Res. Lett.*, *11*, 113–116, doi:10.1029/GL011i002p00113.
Pitzer, K. S., and S. M. Sterner (1995), Equations of state valid continuously from zero to extreme pressures with H_2O and CO_2 as examples, *Int. J. Thermophys.*, *16*, 511–518.
Powell, R., and T. J. B. Holland (1988), An internally consistent dataset with uncertainties and correlations: 3. Applications to geobarometry, worked examples and a computer program, *J. Metamorph. Geol.*, *6*, 173–204.
Reid, M., J. Vazquez, and A. Schmitt (2011), Zircon-scale insights into the history of a Supervolcano, Bishop Tuff, Long Valley, California, with implications for the Ti-in-zircon geothermometer, *Contrib. Mineral. Petrol.*, *161*, 293–311.
Rioux, M., S. Bowring, P. Kelemen, S. Gordon, F. Dudás, and R. Miller (2012a), Rapid crustal accretion and magma assimilation in the Oman-U. A.E. ophiolite: High precision U-Pb zircon geochronology of the gabbroic crust, *J. Geophys. Res.*, *117*, B07201, doi:10.1029/2012JB009273.
Rioux, M., C. J. Lissenberg, N. M. McLean, S. A. Bowring, C. J. MacLeod, E. Hellebrand, and N. Shimizu (2012b), Protracted timescales of lower crustal growth at the fast-spreading East Pacific Rise, *Nat. Geosci.*, *5*, 275–278, doi:10.1038/NGEO1378.
Rioux, M., S. Bowring, P. Kelemen, S. Gordon, R. Miller, and F. Dudás (2013), Tectonic development of the Samail ophiolite: High-precision U-Pb zircon geochronology and Sm-Nd isotopic constraints on crustal growth and emplacement, *J. Geophys. Res. Solid Earth*, *118*, 2085–2101, doi:10.1002/jgrb.50139.
Rioux, M., S. A. Bowring, M. J. Cheadle, and B. E. John (2015), Evidence for excess ^{231}Pa in mid-ocean ridge zircons, *Chem. Geol.*, *397*, 143–156.
Robert, J., C. F. Miranda, and R. Muxart (1969), Mesure de la periode du protactinium-231 par microcalorimetrie, *Radiochim. Acta*, *11*, 104–108.
Robinson, P. T., H. J. B. Dick, and R. P. Von Herzen (1991), Metamorphism and alteration in oceanic layer 3: Hole 735B, in *Proceedings of the Ocean Drilling Program, Sci. Results*, pp. 541–552, Ocean Drilling Program, College Station, Tex.
Rubatto, D., O. Muntener, A. Barnhoorn, and C. Gregory (2008), Dissolution–reprecipitation of zircon at low-temperature, high-pressure conditions (Lanzo Massif, Italy), *Am. Mineral.*, *93*, 1519–1529.
Rusinov, V. L. (1965), On prehnite finds and the clastic nature of epidote in rocks of some areas of contemporary hydrothermal metamorphism, *Izv. Akad. Nauk Kaz. SSR, Ser. Geol.*, *2*, 33–43.
Ryan, W. B. F., et al. (2009), Global Multi-Resolution Topography synthesis, *Geochem. Geophys. Geosyst.*, *10*, Q03014, doi:10.1029/2008GC002332.
Schaltegger, U., T. Pettke, A. Audétat, E. Reusser, and C. A. Heinrich (2005), Magmatic-to-hydrothermal crystallization in the W–Sn mineralized Mole Granite (NSW, Australia). Part I: Crystallization of zircon and REE-phosphates over three million years—a geochemical and U–Pb geochronological study, *Chem. Geol.*, *220*, 215–235.
Schmidt, M. W., and S. Poli (1998), Experimentally based water budgets for dehydrating slabs and consequences for arc magma generation, *Earth Planet. Sci. Lett.*, *163*, 361–379.
Schmitt, A. K. (2007), Ion microprobe analysis of (^{231} Pa)/(^{235}U) and an appraisal of protactinium partitioning in igneous zircon, *Am. Mineral.*, *92*, 691–694.
Schmitt, A. K., M. Grove, T. M. Harrison, O. Lovera, J. Hulen, and M. Walters (2003), The Geysers-Cobb Mountain Magma System, California (Part 1): U-Pb zircon ages of volcanic rocks, conditions of zircon crystallization and magma residence times, *Geochim. Cosmochim. Acta*, *67*, 3423–3442.
Schroeder, T., and B. E. John (2004), Strain localization on an oceanic detachment fault system, Atlantis Massif, 30°N, Mid-Atlantic Ridge, *Geochem. Geophys. Geosyst.*, *5*, Q11007, doi:10.1029/2004GC000728.
Schwartz, J. J., B. E. John, M. J. Cheadle, E. A. Miranda, C. B. Grimes, J. L. Wooden, and H. J. B. Dick (2005), Dating the growth of oceanic crust at a slow-spreading ridge, *Science*, *310*, 654–657.
Schwartz, J. J., B. E. John, M. J. Cheadle, J. L. Wooden, F. Mazdab, S. Swapp, and C. B. Grimes (2010), Dissolution–reprecipitation of igneous zircon in mid-ocean ridge gabbro, Atlantis Bank, Southwest Indian Ridge, *Chem. Geol.*, *274*, 68–81.

Searle, R. (2013), *Mid-Ocean Ridges*, Cambridge Univ. Press, Cambridge.
Searle, R. C., et al. (2010), Structure and development of an axial volcanic ridge: Mid-Atlantic Ridge, 45°N, *Earth Planet. Sci. Lett.*, *299*, 228–241.
Seher, T., W. C. Crawford, S. C. Singh, and M. Cannat (2010), Seismic layer 2A variations in the Lucky Strike segment at the Mid-Atlantic Ridge from reflection measurements, *J. Geophys. Res.*, *115*, B07107, doi:10.1029/2009JB006783.
Sempéré, J.-C., J. Lin, H. Brown, H. Schouten, and G. M. Purdy (1993), Segmentation and morphotectonic variations along a slow-spreading center: The Mid-Atlantic Ridge (24°00′N–30°40′N), *Mar. Geophys. Res.*, *15*, 153–200.
Silantyev, S. A., Y. A. Kostitsyn, D. V. Cherkashin, H. J. B. Dick, P. B. Kelemen, N. N. Kononkova, and E. M. Kornienko (2008), Magmatic and metamorphic evolution of the oceanic crust in the western flank of the MAR crest zone at 15°44′N: Investigation of cores from sites 1275B and 1275D, JOIDES resolution Leg 209, *Petrology*, *16*, 353–375.
Singh, S. C., W. C. Crawford, H. Carton, T. Seher, V. Combier, M. Cannat, J. Pablo Canales, D. Dusunur, J. Escartin, and J. Miguel Miranda (2006), Discovery of a magma chamber and faults beneath a Mid-Atlantic Ridge hydrothermal field, *Nature*, *442*, 1029–1032.
Sinha, M. C., S. C. Constable, C. Peirce, A. White, G. Heinson, L. M. MacGregor, and D. A. Navin (1998), Magmatic processes at slow spreading ridges: Implications of the RAMESSES experiment at 57°45′N on the Mid-Atlantic Ridge, *Geophys. J. Int.*, *135*, 731–745.
Sinton, J. M., and R. S. Detrick (1992), Mid-ocean ridge magma chambers, *J. Geophys. Res.*, *97*, 197–216, doi:10.1029/91JB02508.
Smith, D. K., and J. R. Cann (1992), The role of seamount volcanism in crustal construction at the Mid-Atlantic Ridge (24°–30°N), *J. Geophys. Res.*, *97*, 1645–1658, doi:10.1029/91JB02507.
Smith, D. K., and J. R. Cann (1999), Constructing the upper crust of the Mid-Atlantic Ridge: A reinterpretation based on the Puna Ridge, Kilauea Volcano, *J. Geophys. Res.*, *104*, 25,379–25,399, doi:10.1029/1999JB900177.
Smith, D. K., M. A. Tivey, H. Schouten, and J. R. Cann (1999), Locating the spreading axis along 80 km of the Mid-Atlantic Ridge south of the Atlantis Transform, *J. Geophys. Res.*, *104*, 7599–7612, doi:10.1029/1998JB900064.
Soman, A., T. Geisler, F. Tomaschek, M. Grange, and J. Berndt (2010), Alteration of crystalline zircon solid solutions: A case study on zircon from an alkaline pegmatite from Zomba–Malosa, Malawi, *Contrib. Mineral. Petrol.*, *160*, 909–930.
Spandler, C., J. Hermann, and D. Rubatto (2004), Exsolution of thortveitite, yttrialite, and xenotime during low-temperature recrystallization of zircon from New Caledonia, and their significance for trace element incorporation in zircon, *Am. Mineral.*, *89*, 1795–1806.
Stakes, D., C. Mével, M. Cannat, and T. Chaput (1991), Metamorphic stratigraphy of Hole 735B, in *Proceedings of the Ocean Drilling Program*, *Sci. Results*, pp. 153–180, Ocean Drilling Program, College Station, Tex.
Staudigel, H., and W. Schreyer (1977), The upper thermal stability of clinochlore, $Mg_5Al[AlSi_3O_{10}](OH)_8$, at 10–35 kb P_{H2O}, *Contrib. Mineral. Petrol.*, *61*, 187–198.
Staudigel, H., T. Plank, B. White, and H.-U. Schmincke (1996), Geochemical fluxes during seafloor alteration of the basaltic upper oceanic crust: DSDP sites 417 and 418, in *Subduction Top to Bottom*, pp. 19–38, AGU, Washington, D. C.
Talbi, E. H., J. Honnorez, N. Clauer, F. Gauthier-Lafaye, and P. Stille (1999), Petrology, isotope geochemistry and chemical budgets of oceanic gabbros-seawater interactions in the Equatorial Atlantic, *Contrib. Mineral. Petrol.*, *137*, 246–266.
Tomaschek, F., A. K. Kennedy, I. M. Villa, M. Lagos, and C. Ballhaus (2003), Zircons from Syros, Cyclades, Greece—Recrystallization and mobilization of zircon during high-pressure metamorphism, *J. Petrol.*, *44*, 1977–2002.
Toomey, D. R., S. C. Solomon, G. M. Purdy, and M. H. Murray (1985), Microearthquakes beneath the median valley of the Mid-Atlantic Ridge near 23°N: Hypocenters and focal mechanisms, *J. Geophys. Res.*, *90*, 5443–5458, doi:10.1029/JB090iB07p05443.
Vanko, D. A., and D. S. Stakes (1991), Fluids in oceanic layer 3: Evidence from veined rocks, Hole 735B, Southwest Indian Ridge, in *Proceedings of the Ocean Drilling Program*, *Sci. Results*, pp. 181–215, Ocean Drilling Program, College Station, Tex.
Watson, E. B., and D. J. Cherniak (1997), Oxygen diffusion in zircon, *Earth Planet. Sci. Lett.*, *148*, 527–544.
Watson, E., D. Wark, and J. Thomas (2006), Crystallization thermometers for zircon and rutile, *Contrib. Mineral. Petrol.*, *151*, 413–433.
Wolfe, C. J., G. M. Purdy, D. R. Toomey, and S. C. Solomon (1995), Microearthquake characteristics and crustal velocity structure at 29°N on the Mid-Atlantic Ridge: The architecture of a slow spreading segment, *J. Geophys. Res.*, *100*, 24,449–24,472, doi:10.1029/95JB02399.
Wotzlaw, J.-F., S. K. Hüsing, F. J. Hilgen, and U. Schaltegger (2014), High-precision zircon U–Pb geochronology of astronomically dated volcanic ash beds from the Mediterranean Miocene, *Earth Planet. Sci. Lett.*, *407*, 19–34.